Modeling the RV jitter of early M dwarfs using tomographic imaging

É. M. Hébrard, J. -F. Donati, X. Delfosse, Julien Morin, C. Moutou, I. Boisse

Monthly Notices
of the
ROYAL ASTRONOMICAL SOCIETY

MNRAS **461,** 1465–1497 (2016)
Advance Access publication 2016 June 7

doi:10.1093/mnras/stw1346

Modelling the RV jitter of early-M dwarfs using tomographic imaging

É. M. Hébrard,[1,2,3★] J.-F. Donati,[2,3] X. Delfosse,[4,5] J. Morin,[6] C. Moutou[7,8] and I. Boisse[8]

[1]*Department of Physics and Astronomy, York University, Toronto, ON M3J 1P3, Canada*
[2]*CNRS-INSU; IRAP-UMR 5277, 14 Av. E. Belin, F-31400 Toulouse, France*
[3]*Université de Toulouse, UPS-OMP, IRAP, F-31400 Toulouse, France*
[4]*Univ. Grenoble Alpes, IPAG, F-38000 Grenoble, France*
[5]*CNRS, IPAG, F-38000 Grenoble, France*
[6]*LUPM, Université Montpellier II, CNRS, UMR 5299, Place E. Bataillon, F-34095 Montpellier, France*
[7]*CNRS, Canada-France-Hawaii Telescope Corporation, 65-1238 Mamalahoa Hwy, Kamuela, HI 96743, USA*
[8]*Aix-Marseille Université, CNRS, LAM, UMR 7326, F-13388 Marseille, France*

Accepted 2016 June 2. Received 2016 May 27; in original form 2016 April 1

ABSTRACT

In this paper, we show how tomographic imaging (Zeeman–Doppler imaging, ZDI) can be used to characterize stellar activity and magnetic field topologies, ultimately allowing us to filter out the radial velocity (RV) activity jitter of M dwarf moderate rotators. This work is based on spectropolarimetric observations of a sample of five weakly active early-M dwarfs (GJ 205, GJ 358, GJ 410, GJ 479, GJ 846) with HARPS-Pol and NARVAL. These stars have $v \sin i$ and RV jitters in the range 1–2 km s^{-1} and 2.7–10.0 m s^{-1} rms, respectively. Using a modified version of ZDI applied to sets of phase-resolved least-squares deconvolved profiles of unpolarized spectral lines, we are able to characterize the distribution of active regions at the stellar surfaces. We find that dark spots cover less than 2 per cent of the total surface of the stars of our sample. Our technique is efficient at modelling the rotationally modulated component of the activity jitter, and succeeds at decreasing the amplitude of this component by typical factors of 2–3 and up to 6 in optimal cases. From the rotationally modulated time series of circularly polarized spectra and with ZDI, we also reconstruct the large-scale magnetic field topology. These fields suggest that bistability of dynamo processes observed in active M dwarfs may also be at work for moderately active M dwarfs. Comparing spot distributions with field topologies suggest that dark spots causing activity jitter concentrate at the magnetic pole and/or equator, to be confirmed with future data on a larger sample.

Key words: line: profiles – techniques: polarimetric – techniques: radial velocities – magnetic fields – starspots.

1 INTRODUCTION

Lots of exoplanets were either detected or confirmed thanks to the radial velocity (RV) technique which allows one to detect exoplanets of various masses and sizes, from hot-Jupiters to super Earths. This is made possible thanks to the sensitivity and stability of current velocimeters. However, as an indirect method based on measuring spectral shifts, velocimetry is also sensitive to phenomena of intrinsic stellar origin capable of affecting spectra, and in particular to stellar activity. Whatever the precision of forthcoming instruments, we will remain confronted with this limitation, rendering Earth-like planets hard to detect, their spectral signatures being much smaller than the activity-induced RV jitter, even for weakly active Sun-like stars.

Signals of stellar origin can occur on different time-scales; some have a short period, typically ranging from minutes to hours (e.g. flares, granulation), whereas some feature a longer period, ranging from days to year (e.g. activity cycle, spot or convection inhibition from a strong magnetic field modulated by the rotation). Whatever the temporal time-scale, most stellar phenomena causing spectral variability are related to magnetic fields and to the associated activity demonstrations. The modelling of the RV jitter is essential to all extrasolar planets searches, especially when orbital periods are larger than a few days and when the host stars exhibit activity phenomena occurring on time-scales commensurate with the planetary signals of interest. The only way to improve the sensitivity of RV surveys to small planets is to characterize and model the activity jitter as well as possible.

To diagnose the RV jitter, several complementary approaches are commonly used, mostly making use of chromospheric activity indicators like excess flux in the cores of the Hα and Ca II H&K, or

★E-mail: ehebrard@yorku.ca

measurements of spectral line asymmetries (with the bisector of the cross-correlation function). The idea is to check for periodic modulation of these proxies, in order to assess whether the observed RV signal is caused by activity rather than by a planet (see Queloz et al. 2001). The correlation between RVs and the slope of the bisector can in principle be used to correct for the effect of activity at a level of a few m s^{-1} (Boisse et al. 2009). The accuracy to which the RV jitter can be corrected with this method largely depends on various parameters, e.g. the distribution of spots, the stellar inclination, the rotational broadening of line profiles. An alternative method is based on exploiting complementary information from velocimetric and high-cadence photometric simultaneous/contemporaneous observations, and make use of the predicted relationship between the photometric and RV signatures of spots (Aigrain, Pont & Zucker 2012; Haywood et al. 2014). These studies found that RV modulation caused by spots can be reliably modelled using the photometric flux F and its first derivative F'. Other studies (Meunier, Desort & Lagrange 2010; Borgniet, Meunier & Lagrange 2015) use the Sun as a star to predict the effect of activity on conventional activity diagnostics, taking advantage of the wealth of existing data. However activity, and its correlation to RV jitter, depends strongly on spectral type, stellar mass and rotation rate, and so far, no studies are available to reliably extrapolate the solar case to all types of active stars.

Besides, the large majority of extrasolar planets up to now were found around main-sequence stars of spectral types ranging from late-F to early-M. Despite M dwarfs are the most abundant type of stars, their intrinsic faintness in the visible domain caused them to be underrepresented in RV surveys with existing instruments. RV and transiting survey demonstrate than planets is very frequent around M dwarfs, in particular Earth and super-Earth at short period (Bonfils et al. 2013; Dressing & Charbonneau 2015). Moreover, due to their low masses, these targets are interesting for Earth-like planet hunting; an orbiting planet of a given mass and orbital distance generates a higher reflex motion when orbiting around an M dwarf than around a solar-type star. Therefore, observations of low-mass stars are a promising option to increase our sensitivity to Earth-like planets. Due to the low photospheric temperature of M dwarfs, the planetary orbits that are located in the habitable zone (HZ) of the host star (i.e. within the proper range of orbital distances where liquid water may be stable at the planet surfaces) move closer in. For instance, for an M dwarf with a typical mass of 0.5 $M_{\odot}$ (like those studied in our paper), the HZ lies in a range 0.2–0.45 au (see Kasting et al. 2014). It corresponds to orbital periods in the range 36–157 d, i.e. to RV semi-amplitude of 1.5–0.96 m s^{-1} for a planet mass of 5 $M_{\oplus}$ (as opposed to 0.4 m s^{-1} for a planet of the same mass orbiting in the HZ of a Sun-like star).

Despite the gain in the RV sensitivity to small planets that M dwarfs allow us to achieve, modelling and filtering efficiently the activity jitter of the host stars remain essential, given that this activity jitter is still at best comparable in size to the RV signal we aim at detecting, and with a similar period as orbital periods of planets within the HZ (see e.g. Forveille et al. 2009; Robertson et al. 2014). So far, studies of late-M dwarfs have shown that these stars exhibit significant RV jitter mostly induced by dark spots at their surfaces, implying that efficient observational strategies are mandatory to reliably disclose planets orbiting around them (e.g. Barnes et al. 2014, for M5–M9). These studies rely on simulations and/or spectroscopic and/or photometric survey to diagnose the activity jitter. However, mainly due to their low luminosity in the optical to the near InfraRed (nIR) domain, whether the predominant spot pattern is random, uniform or concentrated at active latitudes remains unclear (Barnes, Jeffers & Jones 2011; Andersen & Korhonen 2015, and references therein). In this paper, we propose to explore a new method based on simultaneously studying the RV jitter caused by activity, and Zeeman signatures reflecting the large-scale magnetic field at the origin of activity to (i) investigate the level to which spot distributions causing the RV jitter relates to magnetic topologies and (ii) devise a new technique based on spectropolarimetric data to filter out activity on a sample of early-M dwarfs.

We present the results of a spectropolarimetric campaign carried out on 2013 September–2014 September. After a brief description of the stellar sample in Section 2.1 and of the data reduction procedure in Section 2.2, we present the results obtained by analysing circularly polarized spectra (Stokes V) in Section 3. The stellar activity diagnostic is introduced in Section 4, and is followed by the analysis of the rotational modulation of the RV jitter, and of its modelling in Section 5. The magnetic field and brightness reconstruction procedure using Zeeman–Doppler imaging (ZDI) are presented in Sections 3.3 and 5.1. We summarize the main outcome of this analysis and discuss its implications in Section 6.

2 SPECTROPOLARIMETRIC OBSERVATIONS

2.1 Stellar sample

Our stellar sample includes five weakly active, early-M dwarfs with different rotation periods (spanning 11–33 d) and stellar masses (0.35–0.61 $M_{\odot}$). The selected targets are among the most observed and best characterized ones in the ESO/HARPS RV survey of M dwarfs (Bonfils et al. 2013), guaranteeing that their activity jitters are known (with rms in the range 2.7–10.0 m s^{-1}) and detectable. So far no planets are detected for the stars of the sample. The five targets are known to show RV variations mostly caused by activity (Donati et al. 2008; Bonfils et al. 2013). The main properties of this stellar sample, both inferred from this work or extracted from previous publications, are listed in Table 1. The sample is complementary to those studied in spectropolarimetry by Donati et al. (2008) and Morin et al. (2008b, 2010).

Stellar masses are derived from the empirical mass–luminosity relationship of Delfosse et al. (2000) together with parallaxes and K-band photometry (both taken from *Hipparcos* catalogue, Koen et al. 2010). The luminosity is deduced from the infrared K-band photometry and $J-K$ colours are converted into luminosities with the bolometric correction of Leggett et al. (2001). The stellar radius $R_{\star}$ is estimated from the mass–radius relation given in Baraffe et al. (2015).

The line-of-sight projected equatorial rotation velocity value ($v \sin i$) is either taken from the literature (Bonfils et al. 2007; Donati et al. 2008; Forveille et al. 2009; Bonfils et al. 2012), or constrained thanks to the ZDI code (see Section 3.3). For the whole sample, the $v \sin i$ is lower than 2 km s^{-1} (see Table 1) and the precision on $v \sin i$ estimate does not exceed 0.5 km s^{-1}. The $v \sin i$ values are compatible with the amount of rotational broadening observed in the spectra of our sample of stars. The measurement of the stellar rotation period $P_{\rm rot}$ is presented in detail in Section 3.2. We found rotation periods ranging from 13.83 to 33.63 d. Finally, the inclination of the rotation axis with respect to the line of sight, i, is estimated from the tomographic technique, with a precision of typically $\pm 10^{\circ}$ (Morin et al. 2010, for more details).

Table 1. Stellar parameters of the M dwarfs sample. Columns 1–8 list the star name, its spectral type (ST), its *J*- and *K*-band magnitude and its distance (coming from the *Hipparcos* catalogue Koen et al. 2010), the stellar mass, luminosity and theoretical radius (Baraffe et al. 2015). The columns 9–12, respectively, list the measured $v \sin i$ (with an estimated error of ± 0.5 km s^{-1}), the assessment of the stellar inclination angle i (with an estimated error of $\pm 10^{\circ}$), the rotation period of the star $P_{\rm rot}$, the rms of RV measurements and the average noise σ_0 on the RV measurements. These four last parameters come from this study.

Name	ST	J	K	Distance (pc)	$M_\star$ ($M_\odot$)	$L_\star$ ($L_\odot$)	$R_\star$ ($R_\odot$)	$v \sin i$ (km s^{-1})	i (°)	$P_{\rm rot}$ (d)	rms$_0$ (m s^{-1})	σ_0 (m s^{-1})
GJ 205	M1	5.0	3.90	5.66 ± 0.04	0.63 ± 0.06	0.061 ± 0.006	0.55 ± 0.08	1	60	33.63 ± 0.37[a]	2.71	1.45
GJ 358	M2	6.90	6.06	9.47 ± 0.15	0.42 ± 0.04	0.023 ± 0.002	0.41 ± 0.06	1	60	25.37 ± 0.32[a]	5.10	2.08
GJ 410	M0	6.52	5.68	11.77 ± 0.15	0.58 ± 0.06	0.055 ± 0.005	0.53 ± 0.08	2	60	13.83 ± 0.10[b]	10.0	3.28
GJ 479	M2	6.86	6.02	9.69 ± 0.22	0.43 ± 0.04	0.025 ± 0.003	0.42 ± 0.06	1	60	24.04 ± 0.75[c]	5.45	2.02
GJ 846	M0	6.20	5.56	10.24 ± 0.16	0.60 ± 0.06	0.059 ± 0.006	0.54 ± 0.08	2	60	10.73 ± 0.10[c]	3.30	2.45

Notes. [a]compatible with Kiraga & Stepien (2007), [b]compatible with Donati et al. (2008), [c]compatible with Bonfils et al. (2012).

Table 2. Main characteristics of NARVAL (Donati 2003) and HARPS-Pol (Snik et al. 2011): column 1 gives the instrument name, column 2 the diameter of the telescope primary mirror, column 3 the spectral domain (covered in a single exposure), column 4 the resolving power R and column 5 the estimated peak instrument throughput η (at ∼550 nm).

Instrument	Tel. (m)	Spectral domain (nm)	R	η (per cent)
NARVAL	2	350–1050	68 000	10–15
HARPS-Pol	3.6	368–691	100 000	2–3

2.2 Instrumental setup and data reduction

Observations presented here were collected during two observing campaigns with the HARPS[1] velocimeter (Mayor et al. 2003; Snik, Kochukhov & Piskunov 2011) used in spectropolarimetric mode and in a smaller extent with the NARVAL[2] spectropolarimeter (Donati 2003; Donati & Landstreet 2009).

We observed from 2013 October to 2014 September with HARPS-Pol. In this instrument two optical fibres convey the stellar light, split into two orthogonal polarization states, from the Cassegrain focus of the telescope to the spectrograph. The instrument covers the 368–691 nm wavelength domain in a single exposure, at a resolving power of 100 000. An additional campaign was carried out from 2013 September to 2014 April with NARVAL, providing full coverage of the optical domain from 350 to 1050 nm in a single exposure, at a resolving power of 65 000, and into two orthogonal polarization states. The main characteristic of the instruments are listed in Table 2.

A spectropolarimetric observation consists of four sub-exposures taken at different azimuths of the quarter-wave plate (for HARPS-Pol)/half-wave rhombs (for NARVAL) relative to the optical axis of the beam splitter. The corresponding frames are combined together to produce a set of Stokes I (unpolarized intensity) and Stokes V (circularly polarized) spectra. Although it is possible to extract polarization spectra from two sub-exposures only, using four allows us to eliminate all systematic errors or spurious polarization signatures at first order (Donati et al. 1997).

The peak signal-to-noise ratios (S/N) per CCD pixel range from 70 to 200 at 600 nm for HARPS-Pol spectra (for which the CCD pixel size is 0.85 km s^{-1}), and from 230 to 480 at 700 nm for NARVAL spectra (for which the CCD pixel size is 2.6 km s^{-1}). It mostly depends on the star magnitude and weather/seeing conditions. An overview of the observations is presented in Table 3, and the detail journal of observations of each star is given in Appendix B.

[1] High Accuracy Radial velocity Planet Searcher and spectropolarimeter at the ESO/3.6 m telescope in La Silla (Chile).
[2] The ESPaDOnS twin at the 2m Telescope Bernard Lyot (TBL) atop Pic-du-Midi (France).

Table 3. Synthetic journal of HARPS-Pol (top panel) and NARVAL (bottom panel) observations. The first days of observation is given in column 2. Column 3 indicates the number of collected spectra. Column 4 lists the peak S/N [respectively, per 0.85 and 2.6 km s^{-1} velocity bin for HARPS-Pol (at 650 nm) and NARVAL (at 750 nm)] – we precise the minimum and maximum obtained values. Column 5 indicates the rotational cycle bounds (computed with the rotation period mentioned in Table 1 according to ephemeris given by equation 1).

Name	BJD$_0$ (+2456000)	$n_{\rm obs}$	S/N	Cycle
GJ 205	569.88	22	170–228	0.000–3.523
GJ 358	675.70	23	70–133	0.000–2.880
GJ 410	673.88	29	79–125	1.000–6.199
GJ 479	778.00	23	63–146	0.024–2.684
GJ 846 (#2)	829.87	11	189–318	25.764–31.848
GJ 205	569.88	4	308–454	1.623–2.186
GJ 410	673.88	13	169–303	0.558–7.542
GJ 846 (#1)	546.46	15	91–158	0.000–8.709

Rotational cycles of each target are computed from Barycentric Julian Dates (BJDs) according to the ephemeris:

$$\mathrm{BJD}(d) = \mathrm{BJD}_0 + P_{\rm rot}.E, \quad (1)$$

in which E is the rotational cycle, BJD$_0$ is the initial date chosen arbitrarily and $P_{\rm rot}$ is the stellar rotation period derived from the magnetic analysis (see Section 3.2).

The data extraction is carried out with LIBRE-ESPRIT, a fully automated dedicated pipeline that performs optical extraction of the spectra. The initial procedure is described in Donati et al. (1997), and was adapted to HARPS-Pol data to make it compliant with precision velocimetry.

We apply least-squares deconvolved (LSD; Donati et al. 1997) to all the observations in order to gather all the available polarimetric information into a single synthetic profile. LSD is similar to cross-correlation in the sense that it extracts information from a large number of spectral lines through a deconvolution procedure (see Donati et al. 1997 for more details). To extract Stokes V LSD profiles from circular polarization spectra, we use a mask of atomic lines computed with an ATLAS local thermodynamic equilibrium model of the stellar atmosphere matching the properties of our whole sample (Kurucz 1993). The final mask contains about 4000 moderate to strong atomic lines, with a known Landé factor, from 350 nm to 1082 nm. The use of atomic lines only for the LSD masks relies on former studies of early and mid-M dwarfs (Donati et al. 2008; Morin

Table 4. Resulting peak flux ratio ρ between NARVAL and Harps-Pol. Column 1 indicates the star name. Column 2 gives ρ computed from spectra, after having taken into account the pixel size differences and the telescope photon collecting power. Column 3 lists ρ obtained from LSD profiles and then this value also takes into account the size of the spectral domain.

	ρ in spectrum	ρ in LSD profile
GJ 205	3.57	5.76
GJ 410	6.32	10.61
GJ846	5.04	8.70

et al. 2008b). Zeeman signatures are clearly detected in Stokes *V* LSD profiles for all stars of our sample with a maximum peak-to-peak amplitude varying from 0.1 to 0.5 per cent of the unpolarized continuum level. We observe temporal variations of the intensity and of the shape of the Stokes *V* LSD profile due to rotational modulation for the whole stars of the sample (see Section 3).

For the unpolarized spectra, we use a denser line mask to increase our sensitivity to profile distortions and to RV variations of these five slow rotators. The mask is derived from M dwarf spectra previously collected with HARPS (Bonfils et al. 2013), and contains 9000 lines from 440 to 686 nm. With this procedure, Stokes *I* LSD profiles distortions are detected with a maximum amplitude varying from 0.001 to 0.01 per cent of the unpolarized continuum level (see Section 5).

For the stars observed with both HARPS-Pol and NARVAL (i.e. GJ 205, GJ 410 and GJ 846), we can use the collected spectra to compare the instrument efficiency. NARVAL being on a 2 m telescope and HARPS-Pol on a 3.6 m telescope, the ratio of the collected flux is about 0.31 at the telescope. The NARVAL peak throughput at 550 nm is thus, *in fine*, about 5.0 times higher than that of HARPS-Pol, once the pixel size is taken into account (see Table 4, second column). LSD allows us to add up information from the whole observed spectral domain. Including the gain associated with the larger spectral domain, NARVAL is in average 8.4 times more efficient than HARPS-Pol (see Table 4, third column). This explains why longitudinal field measurements secured with NARVAL are significantly more accurate than those derived from HARPS-Pol spectra despite the large ratio in telescope photon collecting power in favour of HARPS-Pol. For RV measurements, only HARPS-Pol spectra are used, NARVAL being limited to typical RV precisions of 20 m s^{-1} (Moutou et al. 2007).

3 MAGNETIC ANALYSIS

The goal of this section is to characterize the large-scale magnetic fields of the observed stars from the collected Stokes *V* LSD profiles. To get an overview of the magnetic data, we start by simply computing the longitudinal field B_l, i.e. the line-of-sight projected magnetic vector averaged over the visible stellar hemisphere (Section 3.1). From temporal variations of B_l and its rotational modulation, one can derive a reliable estimate of the stellar rotation period P_{rot} (Section 3.2, and e.g. Morin et al. 2008b). In a second step, we apply ZDI to our time series of Stokes *V* LSD profiles, in order to recover the topology of the large-scale field that generates the observed Zeeman signatures and their rotational modulation (see Section 3.3).

3.1 Longitudinal magnetic field

From each pair of Stokes *I* and *V* LSD profiles, we compute B_l (in Gauss) as follows (Donati et al. 1997):

$$B_l = \frac{-2.14 \times 10^{11}}{\lambda_0 g_{eff} c} \frac{\int v V(v) dv}{\int [I_c - I(v)]\, dv}, \quad (2)$$

with *I* and *V* denoting the unpolarized and circularly polarized LSD profiles, I_c the continuum level, v the RV in km s^{-1}, c, the speed of light in km s^{-1}, λ_0 the central wavelength in nm and g_{eff} the effective Landé factor. B_l is a simple magnetic field proxy one can easily extract, but which conveys little information on the likely complexity of the magnetic field geometry.

3.2 Period determination

To estimate the stellar rotation period we first fit B_l with a multiple sine fit (fundamental period + the first harmonic). The explored period range spans 0.5× to 2× the value found in the literature. We choose P_{rot} that minimizes χ_r^2, defined as the reduced χ^2 of the multiple sine fit to the B_l data. We compare this value to the period found computing the Lomb–Scargle periodogram of the B_l data (Lomb 1976; Scargle 1982; Zechmeister & Kürster 2009). This periodogram estimates the power associated with each period in the explored P_{rot} interval. To assess the chance that the strongest peak of the derived periodogram is caused by noise in the observations rather than by a true signal, we compute the 10 and 1 per cent false alarm probabilities (FAPs) as defined in Zechmeister & Kürster (2009).

(i) GJ 358. The resulting curves for GJ 358 are presented in Fig. 1. We note that B_l remains mainly negative (averaged value of –32.0 ± 1.5 G), with a peak-to-peak amplitude of 70 G. The variations are periodic and well fitted ($\chi_r^2 = 1.0$) with a multiple sine fit at P_{rot}= 25.37 ± 0.32 d (1σ error bar). This period is in agreement with the period of ∼25.26 d given by Kiraga & Stepien (2007) from a photometric survey, as well as with the period found computing the Lomb–Scargle periodogram and associated with an FAP much lower than 1 per cent (Fig. 1, bottom panel).

(ii) GJ 479. We observe a similar behaviour for B_l of GJ 479, with a rotation period of 24.04 ± 0.75 d (see Fig. C1), in good agreement with the period estimated in a range 23–24 d by Bonfils et al. (2012). As indicated in the periodogram of B_l data, and contrary to the previous case, the first harmonic is essential to fit the data down to $\chi_r^2 = 1.0$.

(iii) GJ 410. For GJ 410 (Fig. 2), B_l varies periodically and exhibits regular sign switches; the averaged value is 3.0 ± 0.5 G. The best period we derive from fitting B_l measurements is equal to 13.83 ± 0.10 d, in agreement with the former study of Donati et al. (2008) (13.51 ± 0.12 d) and the Lomb–Scargle periodogram (see Fig. 2, FAP < 1 per cent). This is one of the most active stars of our sample.

(iv) GJ 205. For GJ 205, we derive P_{rot}= 33.63 ± 0.37 d. To fit the data down to $\chi_r^2 = 1.0$, the fundamental period and its first harmonic $P_{rot}/2$ are needed. This is confirmed with the Lomb–Scargle periodogram whose strongest peak is at 16.8 d, i.e. $P_{rot}/2$ (FAP < 1 per cent, see Fig. C2), and with the former photometric study of Kiraga & Stepien (2007) (∼33.61 d).

(v) GJ 846. For GJ 846, we only secured 11 measurements in 2014 July–September with HARPS-Pol and 15 measurements in 2013 September–December with NARVAL, spread over 6 and 9 rotation cycles, respectively. The amplitude of the B_l variations changes between the two observation epochs: we first observe variations with a peak-to-peak amplitude of 10 ± 2 G (averaged value

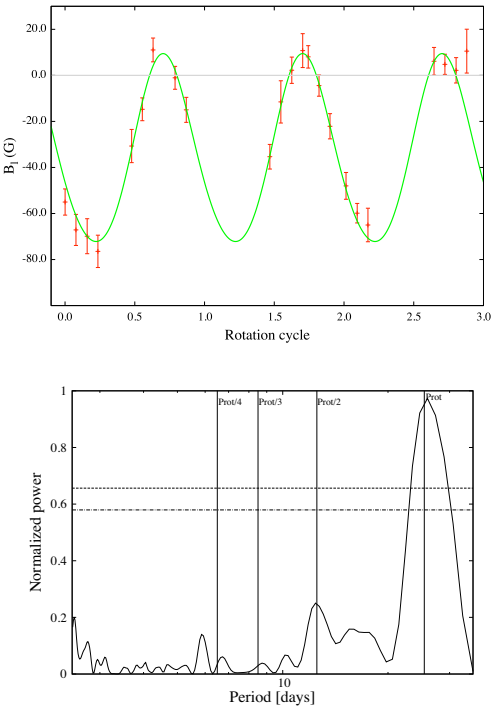

Figure 1. Top: B_l measurements of GJ 358 from HARPS-Pol spectra are shown as red dots (with $\pm$ 1σ error bars). The green line depicts a multiple sine fit (fundamental + first harmonic) to the B_l measurements. The horizontal grey line represent the 0 G level. Bottom: Lomb–Scargle periodogram of B_l and the FAP at 1 per cent (dashed line) and 10 per cent (dot–dashed line). The vertical lines depict P_{rot} and its three first harmonics $P_{rot}/2$, $P_{rot}/3$ and $P_{rot}/4$.

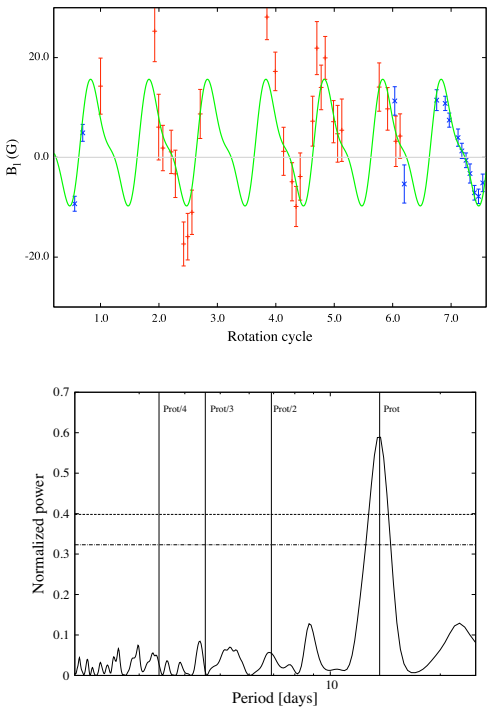

Figure 2. Same as Fig. 1 for GJ 410. Measurements from HARPS-Pol spectra are shown in red, while those from NARVAL spectra are shown in blue. Note the much smaller error bars on NARVAL B_l measurements, despite the 3.2$\times$ smaller photon collecting power of TBL.

1.4 $\pm$ 0.5 G), then variations with a peak-to-peak amplitude of 20 $\pm$ 4 G (averaged value = 6.0 $\pm$ 1.5 G). B_l keeps the same (positive) sign during the two runs. We derive a period equal to 10.73 $\pm$ 0.10 d. This period is in good agreement with the periodicity of 10.7 d found in Bonfils et al. (2012).

Our observations thus demonstrate clearly that the spectropolarimetric data provides us with an accurate measurement of P_{rot}. In Section 4, we will demonstrate that spectropolarimetry is more efficient that usual proxies (Hα or the full width at half-maximum, FWHM) to determine the rotational period, and that P_{rot} is a key parameter to track the origin of the activity signal (i.e. the magnetic field).

3.3 Magnetic imaging

To recover the parent large-scale magnetic field from time series of rotationally modulated Zeeman signatures, we use the ZDI tomographic imaging technique. ZDI has been largely tested and improved since the initial release of Brown et al. (1991) (see e.g. Donati et al. 2006b; Morin et al. 2008b). ZDI assumes that profile variations are mainly due to rotational modulation (plus some amount of differential rotation, if needed), and can turn series of circular polarization Stokes V LSD profiles into maps of the parent magnetic topology. The longitudinal and latitudinal resolution depends mainly on $v \sin i$, i, and the phase coverage of the observations.

In our imaging procedure, we use spherical harmonics (SH) to describe the large-scale field, allowing in particular to reliably recover both simple and complex topologies (see e.g. Donati 2001; Donati et al. 2006b). $\boldsymbol{B}$ can be written as the sum of a poloidal and a toroidal component; their expressions can be found in Donati et al. (2006a). The parameters $\alpha_{l,m}$, $\beta_{l,m}$ and $\gamma_{l,m}$, noting the SH coefficients (with l denoting the degree of the mode, and $m \in [\,0\,;\,l\,]$ its order), describe, respectively, the radial poloidal, non-radial poloidal and toroidal components of the magnetic field. The energy associated with the axisymmetric ($m < l/2$) and non-axisymmetric modes of the poloidal field component, as well as that of the poloidal and toroidal components, can be estimated directly from the coefficients of the SH expansion. For the slow rotators considered here, most spatial information we can recover about the field concentrates in modes with orders equal to or lower than 5 (see e.g. Morin et al. 2008b).

To compute synthetic circular polarization profiles, the surface of the star is divided into 5000 cells of similar projected areas (at maximum visibility), whose contribution to the integrated Stokes I and V LSD profiles depends on the RV of each cell, on the local field strength and orientation, on the location of the cell and its projected area, on the rotation cycle, and on the local surface brightness of the photosphere (assumed to be uniform at this stage). To model the local unpolarized Stokes I and the local circular polarized Stokes V profiles (respectively, $I_{l,j}$ and $V_{l,j}$) at each cell j in presence of magnetic fields, we use Unno–Rachkovsky's (UR's) equations (e.g. Landi degl'Innocenti & Landolfi 2004). We set the central wavelength, the Doppler width and the Landé factor of the equivalent line to 650 nm, 1.6 km s^{-1} and 1.25, respectively, and we adjust the average line-equivalent width to the observed value. Summing the spectral contributions of all grid cells yield the synthetic Stokes V profiles at a given rotation phase.

ZDI proceeds by iteratively comparing the synthetic profiles to the observed ones, until they match within the error bars. Since the inversion problem is ill-posed, ZDI uses the principles of

Table 5. Properties of the large-scale magnetic field topologies of the moderately active M dwarfs sample. In columns 1–3, we report the name of the star (with runs #1 and #2 for GJ 846 corresponding to the first and second observing epochs, see Table B4), the mass and the rotation period, initially presented in Table 1. Column 4 mentions the assessment of the average magnetic flux reconstructed from the Zeeman signatures. Column 5 lists the magnetic energy lying in poloidal component. Columns 6 and 7 present the magnetic energy reconstructed as a poloidal dipole and the percentage of poloidal energy in axisymmetric modes (defined as $m < l/2$).

Name	$M_\star$ ($M_\odot$)	$P_{\rm rot}$ (d)	B_V (G)	Pol. (%)	Dip. (%)	Axi (%)
GJ 205	0.61	33.63 ± 0.37	20	99	90	73
GJ 358	0.41	25.37 ± 0.32	130	97	98	85
GJ 410	0.58	13.83 ± 0.10	65	25	88	11
GJ 479	0.43	24.04 ± 0.75	65	37	74	29
GJ 846 (#1)	0.59	10.73 ± 0.10	45	27	69	68
GJ 846 (#2)	0.59	10.73 ± 0.10	30	63	52	86

maximum-entropy image reconstruction to retrieve the simplest image compatible with the data. The form we use for the regularization function is $S = \sum_{l,m} l(\alpha_{l,m}^2 + \beta_{l,m}^2 + \gamma_{l,m}^2)$ (more details in Donati 2001).

ZDI depending on the assumed rotation period, it can be used to confirm and often to improve the accuracy of the estimate derived from B_l curves, as Stokes V profiles intrinsically contain more information than B_l curves. In some cases, surface differential rotation (DR) is required in order to fit Stokes V data down to the noise level. To achieve this, we assume that the rotation rate at the surface of the star depends on latitude and can be expressed as $\Omega(\theta) = \Omega_{\rm eq} - {\rm d}\Omega \sin^2(\theta)$, with θ denoting the latitude, $\Omega_{\rm eq}$, the rotation rate at the equator and dΩ, the difference in rotation rate between the equator and the pole. This law is used to compute the phase shift of each ring of the grid at any observation epoch with respect to its position at a reference epoch. We carry out reconstructions for a range of $\Omega_{\rm eq}$ and dΩ values; the optimum DR parameters are those minimizing the information content. They are obtained by fitting the surface of the χ_r^2 map with a paraboloid around the minimum value (Donati, Collier Cameron & Petit 2003).

3.4 Results

The M dwarfs of our sample exhibit magnetic fields with Zeeman signatures that do not exceed 0.5 per cent of the unpolarized continuum. We distinguish two kinds of magnetic topologies (see Table 5): two stars harbour a large-scale magnetic field dominated by an axial dipole (GJ 358, GJ 205), whereas three stars exhibit a more complex field featuring a significant – in most case dominant – toroidal axisymmetric component (GJ 410, GJ 479 and GJ 846).

(i) GJ 358 and GJ 205. For the stars whose large-scale field is mostly poloidal, the Stokes V LSD signatures are mainly antisymmetric with respect to the line centre. Their shape remain mostly constant (see e.g. GJ 358 in Fig. 3), but their intensity vary significantly as the star rotates (see *e.g.* the rotation cycles 0.235 and 0.789 in Fig. 3 top panel). For these stars, the reconstructed magnetic topologies are simple with more than 90 per cent of the magnetic energy concentrated in a dipolar poloidal component (i.e. SH mode with $l = 1$, see column 6 of Table 5). The Stokes V LSD signatures are fitted down to a $\chi_r^2 \sim 1$, from an initial value (corresponding to a null field map) of ∼3.5–3.1 (depending on the S/N ratio and on the number of collected data). In the most magnetic regions, the flux reaches 230 G at the surface of GJ 358, but only 30 G at the surface of GJ 205 (see Fig. D1).

(ii) GJ 479 and GJ 410. For the stars with a significant toroidal component, the Stokes V LSD profiles have a sign that varies during the stellar rotation (see *e.g.* the rotation cycles 2.067 and 2.493 of GJ 410 in Fig. 4 top-left panel). The large-scale magnetic field reconstruction indicates that the axisymmetric poloidal component includes less than 40 per cent of the magnetic energy (see column 7 of Table 5), and features a mostly dipolar structure ; the toroidal component includes more than 60 per cent of the reconstructed magnetic energy, and is mostly axisymmetric, showing up as an azimuthal field ring of ∼ 80 G encircling the star at equatorial or intermediate latitudes (see Table 5, two last rows, and Figs 4 and D2 bottom panel, for, respectively, GJ 410 and GJ 479). The magnetic field flux is moderate, reaching ∼ 70 G in the in the strongest field regions.

Moreover, thanks to the dense spectropolarimetric data set of GJ 410 (42 measurements spread over 7.5 rotation cycles), we can easily estimate the amount of latitudinal DR shearing the magnetic maps. Indeed, the Stokes V LSD data set of all stars of our sample can be fitted down to $\chi_r^2 = 1$ when assuming solid body rotation, except for GJ 410 ($\chi_r^2 = 1.6$). Assuming DR, we are able to fit the data of this early-M dwarf down to $\chi_r^2 = 1.0$, with $\Omega_{\rm eq} = 0.47 \pm 0.03$ rad d^{-1} and ${\rm d}\Omega = 0.05 \pm 0.03$ rad d^{-1} (see Fig. 5), corresponding to rotation periods at the equator and pole of 13.37 ± 0.86 and 14.96 ± 1.25 d, respectively. This result is in good agreement with $P_{\rm rot}$ previously found (13.83 ± 0.10 d, Section 3.2), and with the former DR estimate of GJ 410 (see Donati et al. 2008).

Finally, we note that the large-scale field of GJ 410 significantly evolved between 2007–2008 (Donati et al. 2008) and 2014 (our data), both in strength (decreasing from 100 to 60 G) and in topology (the energy in the dipolar component increased from 50 to 88 per cent).

(iii) GJ 846. For GJ 846, we notice a variability of the large-scale magnetic topology between 2013 and 2014, as expected from the B_l analysis (Section 3.2). More specifically, the energy in the poloidal component increases from 27 per cent in 2013 to 63 per cent in 2014 (see Fig. D3, middle and bottom panels),

Early-M dwarfs like GJ 410 and GJ 846 were already reported to be prone to increased variability, probably as a result of their stronger surface DR (see Donati et al. 2008; Morin et al. 2008a,b).

4 CHARACTERIZATION OF THE RV JITTER

Our sample stars are known to exhibit RV variations caused by stellar activity. To characterize the origin of the RV modulation, we compute the bisector, the FWHM, and the Hα index as described in Section 4.1. We then analyse how these quantities vary with time through their Lomb–Scargle periodograms, and compare with temporal variations of the RV itself (see Section 4.2.1). As the model we propose aims at modelling the component of the RV signal that is rotationally modulated (see Section 5), the first step is to assess quantitatively the amount to which the RVs of our sample stars are periodic (see Section 4.2.2).

4.1 Computing RVs and activity proxies

RVs are computed by fitting a Gaussian to the Stokes I LSD profiles (equivalent to the cross-correlation function (CCF)), the Gaussian centroid giving the RV estimate $v_{\rm r}$. The FWHM measurements is directly computed from the Gaussian fit to the Stokes I LSD profiles.

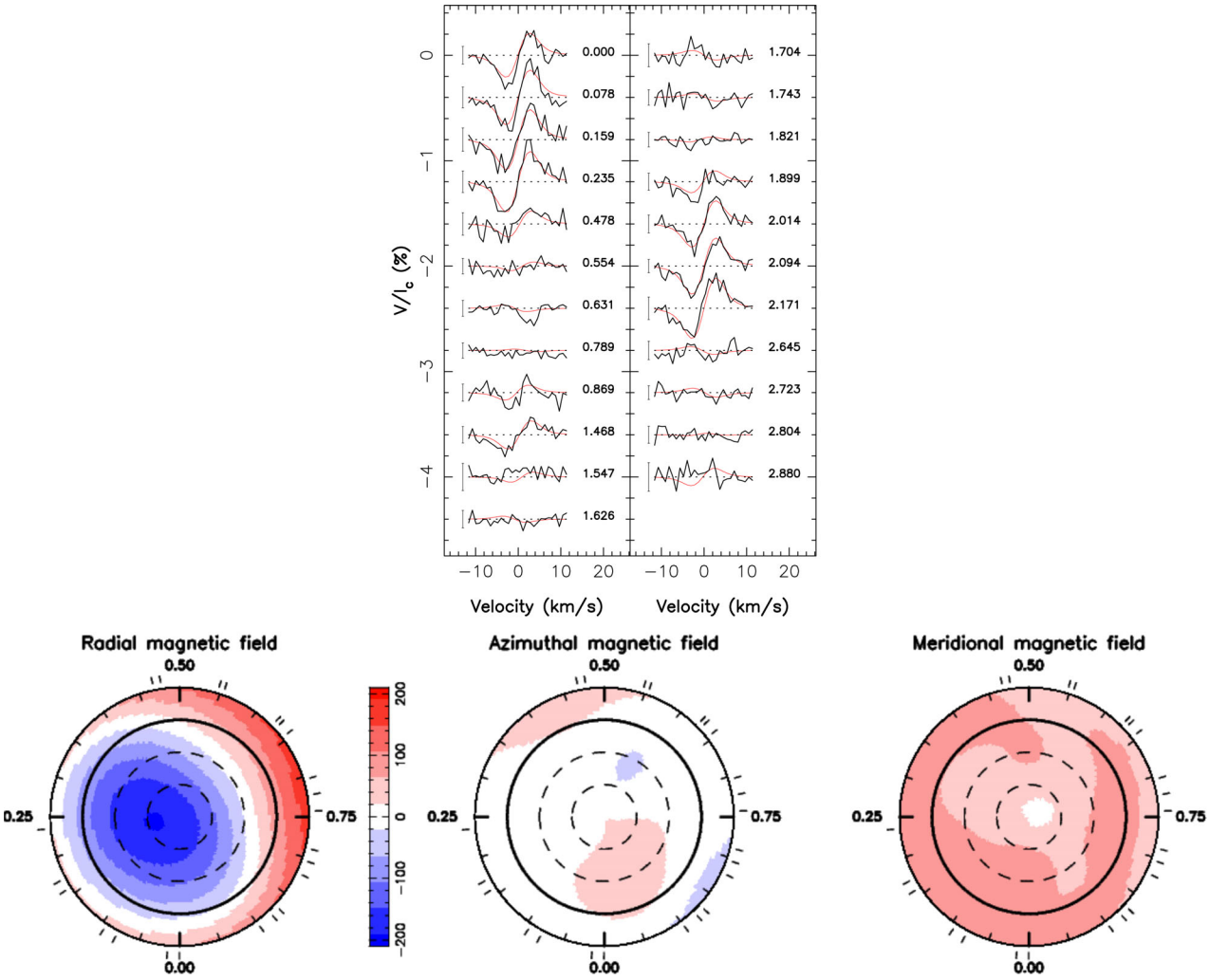

Figure 3. Top: maximum-entropy fit (thin red line) to the observed (thick black line) Stokes *V* LSD photospheric profiles of GJ 358. Rotational cycles and 3σ error bars are also shown next to each profile. Bottom: map of the large-scale magnetic field at the surface of GJ 358. The radial (left-hand corner), azimuthal (centre) and meridional (right-hand corner) components of the magnetic field *B* are shown. Magnetic fluxes are labelled in G. The star is shown in a flattened polar projection down to latitude $-30°$, with the equator depicted as a bold circle and parallels as dashed circles. Radial ticks around each plot indicate phases of observations.

To derive the bisector, we first interpolate the CCF profile using a cubic spline interpolation; we then compute the set of mid-points of horizontal line segments extending across the profile (Gray 1982). To assess temporal evolution of the line profile, we calculate the velocity span (as introduced, e.g. by Gray 1982 and Queloz et al. 2001) v_s, given by $v_t - v_b$, where v_t and v_b are, respectively, the average velocity at the top and bottom parts of the bisector[3]. For RV variations caused by stellar activity, we commonly observe an anticorrelation between v_s and v_r (see e.g. Queloz et al. 2001). However, as expected for slow rotators whose rotation profile is not resolved by the velocimeter (typically $v \sin i < 2$ km s^{-1}, see e.g. Desort et al. 2007), this v_s versus. v_r anticorrelation is not observed in our sample, v_s exhibiting no variations (for example, for GJ 358, v_s has a peak-to-peak amplitude of $\sim$10 m s^{-1} and an rms of 3.6 m s^{-1}, see Fig. 6). For this reason, this proxy is not discussed in the following sections, even though v_s is computed and shown in Fig. 6 and similar following graphs.

The Hα index is also often used to characterize RV variations caused by activity. This index is defined as the ratio between the flux in the Hα absorption line and that in the surrounding continuum, as described in Boisse et al. (2011). We use a 0.16 nm window centred at 656.2808 nm for the central line, and two windows of 1.075 and 0.875 nm around 655.087 and 658.031 nm, respectively, for the continuum as presented in Gomes Da Silva et al. (2011).

[3] The top and bottom parts include all points within 10–40 and 60–90 per cent of the full line depth, respectively.

4.2 Activity jitter in the M dwarfs sample

4.2.1 Diagnostic of the activity

Only 11 RV measurements spanning 5.4 rotation cycles were collected for GJ 846 (run #2) – too sparse a set for a reliable periodogram analysis. As a result, the following sections concentrate only on the four other stars of the sample, namely GJ 358, GJ 479, GJ 410 and GJ 205.

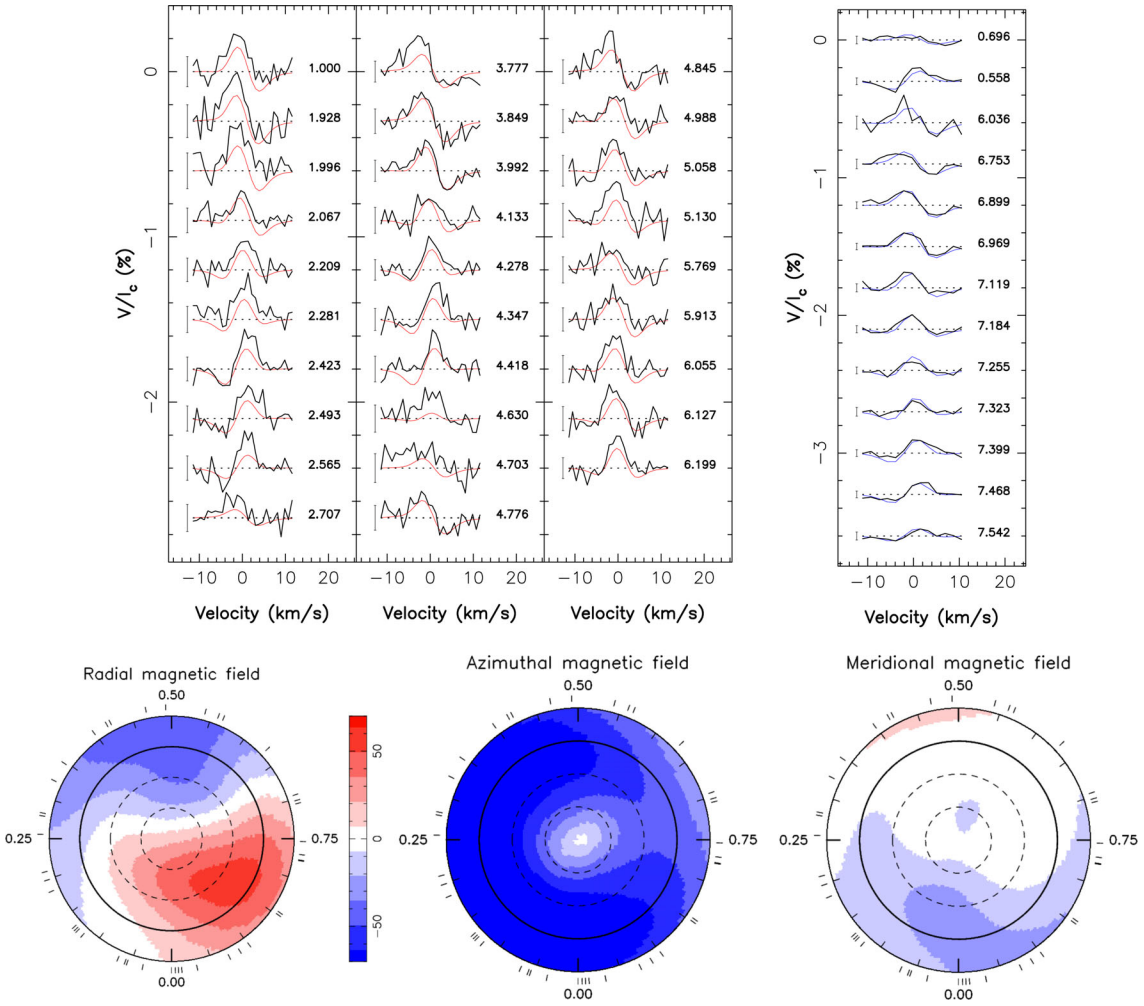

Figure 4. Same as Fig. 3 for GJ 410. LSD Stokes *V* profiles in the top-left and top-right panels correspond to HARPS-Pol and NARVAL observations, respectively.

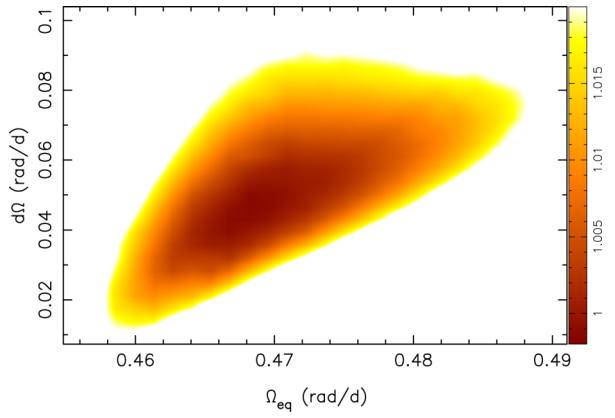

Figure 5. Variations of χ_r^2 as a function of Ω_{eq} and dΩ, derived from the modelling of GJ 410 Stokes *V* LSD profiles at constant information content. The outer colour contour traces the 1.75 per cent increase in χ_r^2 that corresponds to a 3σ ellipse for both parameters as a pair.

(i) GJ 358. The B_l, RV, FWHM, Hα and v_s curves as well as the periodograms of B_l, RV, FWHM and Hα are presented in Fig. 6. The periodograms of both Hα and FWHM show that the period P_{rot} previously identified with B_l has significantly more power than its harmonics (FAP < 1 per cent for FWHM, < 15 per cent for Hα). It is a further confirmation that the observed RV modulation is mainly caused by activity. The periodogram of v_r indicates a period of $P = 24.47 \pm 0.60$ d, in agreement with P_{rot}, but with an FAP of only 10 per cent. Moreover, we notice that v_r and B_l vary in quadrature: when B_l reaches its maximum value (of about +10 G), v_r is at mid-distance between its maximum and minimum (see e.g. phases 0.70–0.75).

(ii) GJ 479. Hα and FWHM show variations with a period in the range 23–25 d, in agreement with the P_{rot} that we previously derived from our B_l data. RVs allow us to measure a period of 23.2 $\pm$ 1.9 d, again fully compatible with P_{rot} (see Fig. E1). Moreover the Hα periodogram exhibits a similar harmonics spectrum (from P_{rot} to $P_{rot}/4$) as those of B_l and v_r. Furthermore the shape of v_r and B_l curve are very similar, in particular v_r crosses its median value when B_l is close to zero (see e.g. phase 0.45).

(iii) GJ 410. Being the most active star of our sample, GJ 410 exhibits the largest temporal variations for all proxies (typically $\times$1.5, see Fig. 7). The periodogram of v_r indicates a period $P = 14.20 \pm 0.20$ d, within the range of surface periods that DR triggers (13.4–15.3 d, see Section 3.4). The period measured with v_r being higher than P_{rot} measured with B_l, this suggests that the surface spots generating the observed RV variations are located at mid to high latitudes.

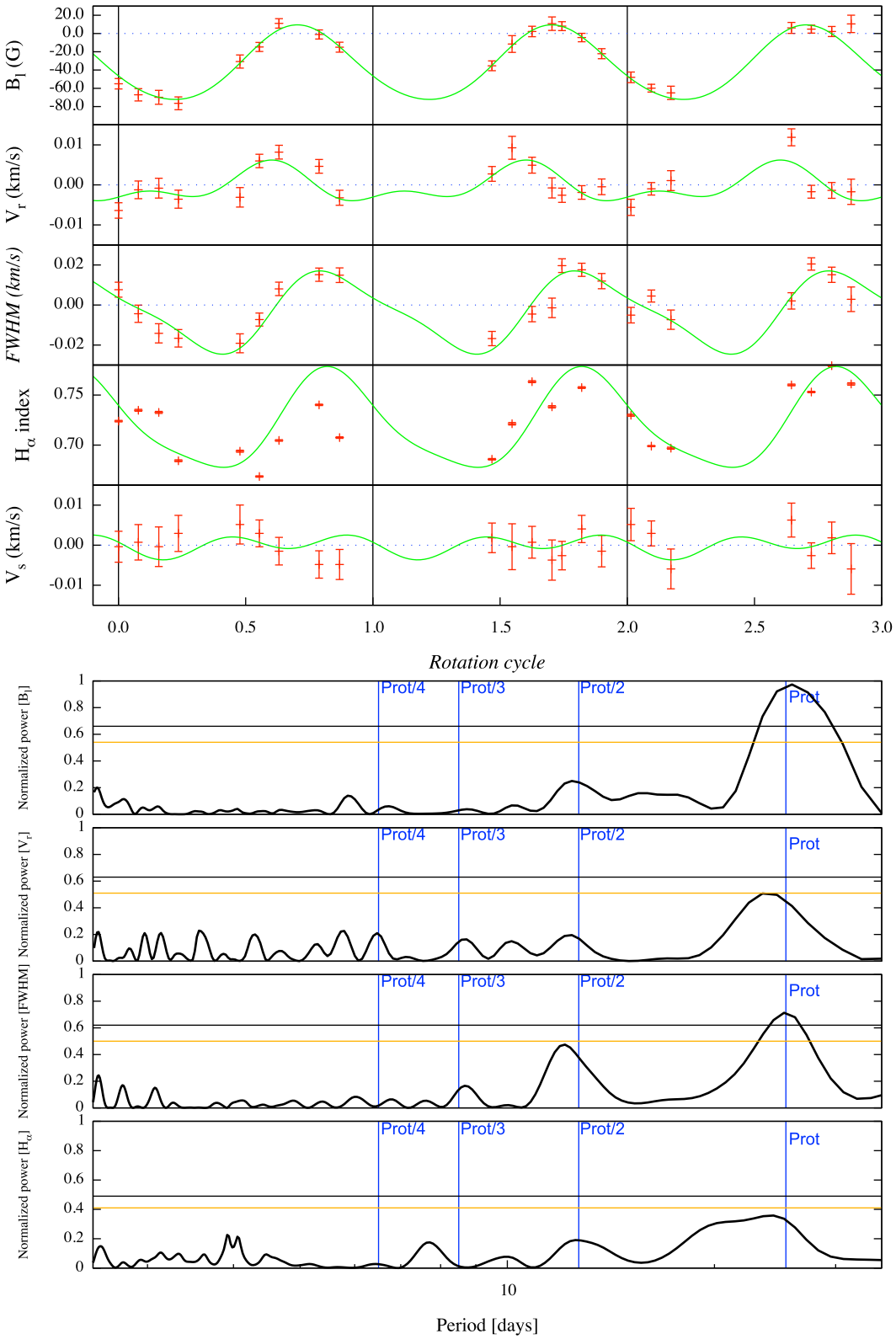

Figure 6. Top: Temporal variations of B_l, v_r, FWHM, Hα and v_s for GJ 358. Data and their error bars are in red. For all plots, the zero level is depicted by a dotted line. The green lines depict a multiple sine fit (including the fundamental at P_{rot} and first harmonic at $P_{rot}/2$) to the data points. The vertical black lines outline the beginning of each rotation cycle. Bottom: Lomb–Scargle periodograms of B_l, v_r, FWHM and Hα for GJ 358. The blue vertical lines outline the rotation period P_{rot} and its first 3 harmonics at $P_{rot}/2$, $P_{rot}/3$ and $P_{rot}/4$. The yellow and black horizontal lines, respectively, mark FAP levels of 10 and 1 per cent.

Table 6. Table of the parameter that characterize the detection and the multiple sine fit of the RV activity jitter. The first column gives the name of the star, columns 2–4 give the observed average RV noise σ_0, the rms of the RV data rms_0, and the associated χ^2_r, $\chi^2_{r,0}$. Columns 5 and 6 mention the rms of the RV residual obtained after a multiple sine-fit (fundamental + 2 harmonics), the χ^2_r associated with the fit $\chi^2_{r,1}$. Column 7 lists the estimate of the likelihood of the fit (FAP, see text). Columns 8–10 give the rms of the RV residuals after the DI modelling, the associated χ^2_r, and the FAP. Columns 11–13 list the initial and final χ^2_r linked to the *RI* reconstruction, and the associated FAP.

	Raw RV data			Multiple sine fit (fond. + 2 harm.)			DI modelling					
							RV curve			LSD profiles		
	σ_0 (m s^{-1})	rms_0 (m s^{-1})	$\chi^2_{r,0}$	rms_1 (m s^{-1})	$\chi^2_{r,1}$	FAP (%)	rms_2 (m s^{-1})	$\chi^2_{r,2}$	FAP (%)	$\chi^2_{r,i}$	$\chi^2_{r,f}$	FAP (%)
GJ 205	1.45	3.52	7.81	3.05	6.27	73	3.17	6.31	98	4.3	3.8	75
GJ 410	3.28	8.84	7.85	6.55	3.96	0.04	6.78	4.14	2.8	2.9	2.0	≤0.01
GJ 479	2.02	5.29	7.71	3.65	3.58	0.09	3.93	4.05	7.4	5.0	2.9	≤0.01
GJ 358	2.08	4.79	5.59	2.47	1.69	≤0.01	2.88	2.05	≤0.01	3.8	2.1	≤0.01

(iv) GJ 205. The data and their periodograms are presented in Fig. E2. The Hα periodogram shows a main peak at 33.46 d with an FAP $\leq$ 15 per cent. This period is consistent with the P_{rot} derived from B_{l} and mentioned in Kiraga & Stepien (2007) (33.63 $\pm$ 0.37 d and 33.61 d respectively), and confirms that the observed signals are due to stellar activity. FWHM measurements do not allow us to firmly identify the rotation period of the star, and no signal with the P_{rot} derived from B_{l} is detected in v_{r} with an FAP of 98 per cent. The strongest peak in v_{r} periodogram is at 39.70 $\pm$ 0.85 d and not compatible with P_{rot}. However, GJ 205 being an early-M dwarf, one can assume that it features a similar amount of DR to that observed on GJ 410, i.e. $\mathrm{d}\Omega = 0.05$ rad d^{-1}. This level of DR would correspond to a difference of 10 d between the polar and the equatorial rotation periods, and would thus allow us to reconcile the observed peaks in the different periodograms. If confirmed, this would suggest that dark spots are located at high latitudes. Unfortunately, the present data set does not allow us to measure the DR, and to further confirm this assumption.

Comparing the period derived from B_{l} and those derived from RV, FWHM and Hα (see Table A1) demonstrates that the rotation period of the star is most of the time more efficiently determined through B_{l} data than through RVs or other usual activity proxies (high FAP). In our small sample, we find that the different period values are in agreement for GJ 358 and GJ 479. We thus can suspect a solid rotation and/or that the strongest magnetic area and the spots are at similar latitudes. For GJ 410, the periods differ but are in agreement with the DR we measured from the magnetic data. Finally, for GJ 205, we suspect a DR effect, but we cannot measure with the current data set.

This preliminary analysis demonstrates that most of our sample stars show rotationally modulated RVs, whose variations are obviously linked with those of the longitudinal field and other activity proxies. By comparing these different values of period, we can thus further investigate the origin of the observed RV jitter.

4.2.2 RV signal detection

The rms of the data (rms_0) is 2–3× higher than the average noise σ_0. The multiple sine fit (including the 2 first harmonics) to the RV data allows us to improve χ^2_r with respect to a fit with a constant RV, however we never reach $\chi^2_r = 1.0$ (see Table 6, 7 first columns). This suggests that the RV jitter, J_{tot}, includes both a rotationally modulated component J_{m} (due, e.g. to long-lived spots at the stellar surface), as well as a randomly varying one J_{r} (of yet unclear origin, e.g. spots with lifetimes shorter than the rotation cycle). Their respective strengths vary from one star to the other. For example, the poorest fit to the data are that of GJ 205, whose period in the RV data significantly differs from P_{rot} (determined from the magnetic data, see Section 3.2) and for which periodicity in the v_{r} signal is not really detected.

Multiple sine fits and Doppler imaging (see Section 5) can only succeed at modelling signals varying periodically with P_{rot}; our first task is thus to quantify the extent to which the observed RV signals are indeed mostly modulated by rotation. We thus compute the probability that a multiple sine fit provides a significantly better match to the observed RV variations than does a constant RV. We use the incomplete Gamma function to assess this probability p, given both the number of degrees of freedom and the improvement in χ^2_r that a multiple sine fit (including 2 harmonics) provides with respect to a constant RV. The closer p gets to 1.0 and the false alarm probability (FAP $= 1-p$) to 0, the more reliably the rotational modulation of the RV signal is detected and dominates the RV variations. As we test the ability of the model to fit the rotationally modulated component J_{m}, we use a scaled $\Delta\chi^2$ given by

$$\Delta\chi^2 = \frac{\chi^2_{r,0} - \chi^2_{r,1}}{\chi^2_{r,1}} N, \tag{3}$$

where N denotes the number of measurements. The resulting FAP are gathered in Table 6. We note that for GJ 358, GJ 479 and GJ 410, J_{m} is dominant with an FAP level of <1 per cent, whereas for GJ 205 J_{r} largely dominates the signal (with an FAP level of ∼73 per cent[4]), so that for this star no coherent signal is detected at the rotation period measured from B_{l}.

To quantify the strength of J_{m} and J_{r}, we compute their rms, once having quadratically subtracted the noise (see Table 7). Whereas J_{m} is the major component for GJ 358 and, in a smaller extend for GJ 479, the trend is reversed for GJ 205 and GJ 410, where J_{r} becomes dominant. The Doppler imaging being able to model the rotational modulation only, we aim at reduce the activity jitter by a factor A_1.

5 MODELING OF THE RV JITTER

The goal of this section is to consistently model the rotationally modulated component of the activity jitter (called J_{m} in Section 4.2.2) and translate it into a distribution of surface features,

[4] However if we assume that DR is present at the surface of GJ 205 (at a level similar to that reported for GJ 410) and is responsible for modulating the RV data with a period of 39.70 $\pm$ 0.35 d (rather than that of 33.63 $\pm$ 0.37 d derived from the magnetic data), the FAP level drops down to 2 per cent.

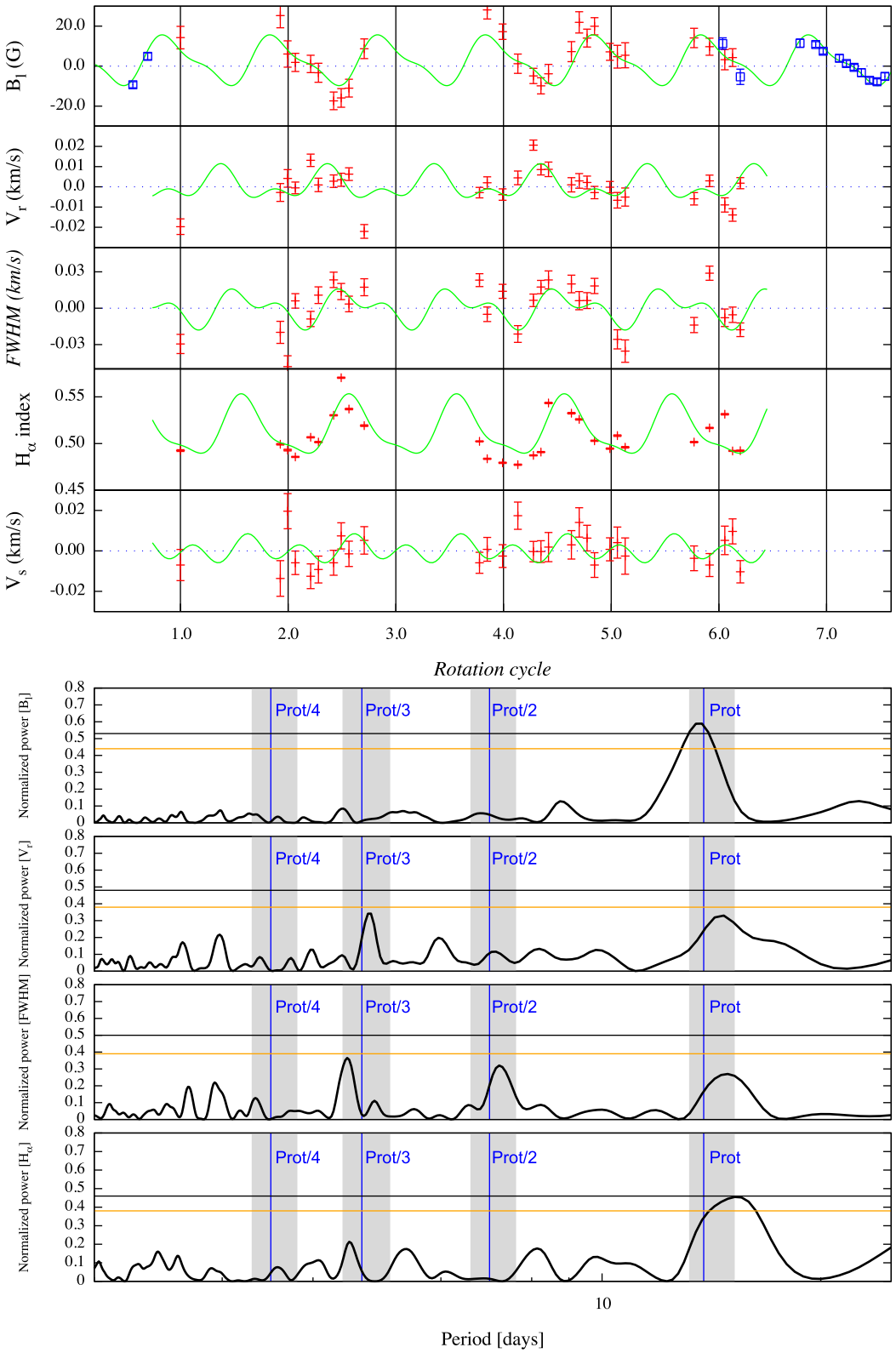

Figure 7. As Fig. E1 for GJ 410. The blue data are the B_l values computed from NARVAL LSD profiles. The grey bands depict the range of periods at the surface of the star as a result of DR.

whose relation to the parent magnetic topology (described in Section 3.4) can be studied – at least on a statistical point of view.

For this first approach, we assume that the distortions observed in Stokes *I* LSD profiles are only due to rotational modulation induced by spots. On the stellar surface, two kinds of features can be found: hot/bright plages and cool/dark spots. These features induce an RV activity jitter and variations of the bisector span. When the contribution of spots is dominant, the amplitude of the RV variations

Table 7. The first column indicates the name of the star. Column 2 gives $\mathrm{rms}_{J,\,\mathrm{tot}}$, the rms of the RV data, once the noise has been quadratically subtracted ($J_{\mathrm{tot}} = \sqrt{\mathrm{rms}_0^2 - \sigma_0^2}$, with rms_0, the rms of the data, see Table 6). Column 3 mentions J_{m}, the rms of the RV jitter due to rotational modulation ($J_{\mathrm{m}} = \sqrt{\mathrm{rms}_0^2 - \mathrm{rms}_1^2}$). Column 4 indicates the rms of the random component of the RV jitter, J_{r} ($J_{\mathrm{r}} = \sqrt{\mathrm{rms}_1^2 - \sigma_0^2}$). With a model of the rotational modulation only, we can reduce the activity jitter by a factor $A_1 = J_{\mathrm{tot}}/J_{\mathrm{r}}$ (column 5).

	J_{tot} (m s^{-1})	J_{m} (m s^{-1})	J_{r} (m s^{-1})	A_1
GJ 205	3.21	1.75	2.68	1.2
GJ 410	8.21	5.67	5.93	1.4
GJ 479	4.89	3.83	3.04	1.7
GJ 358	4.31	4.10	1.33	3.2

is higher than those of the bisector span, and when the contribution of plages is dominant, the amplitude of the RV variations is similar to or smaller than those of the bisector span (Dumusque, Boisse & Santos 2014, equation 10). In our sample, v_{s} data do not exhibit a peak-to-peak amplitude higher than 15 m s^{-1} and we do not observe any clear v_{s} variations (see Section 4.1), whereas the peak-to-peak amplitude of RV variations is always higher than 15 m s^{-1}. Moreover, thanks to 3D simulations of the near-surface convection of M dwarfs that take into account the small-scale magnetic field, Beeck et al. (2015) show that dark spots are much more abundant than plages. Thus, at first order, we consider dark spots only as the main origin of the observed rotationally modulated RV variations.

In the imaging procedure, we characterize a spot with its relative brightness b, and its local profile I_{s}. This two parameters being fixed, we adopt a simple two-temperature model (warm photosphere, cool spots) for the stellar surface and we choose the spot covering fraction as image parameter.

5.1 Method

As previously presented for the magnetic field reconstruction, the stellar surface is divided into 5000 cells, and the Stokes *I* profile at a given rotation phase is computed as the sum of all local Stokes *I* profiles from the different cells. With the spot description we chose, the parameter we reconstruct during the ZDI process is $1 - C_j$, with C_j denoting the proportion of photosphere inside each cell ($C_j = 0$ and $C_j = 1$, respectively, corresponding to a spotted cell, and to an unspotted cell), and therefore, the local profile I_j of the cell j is given by

$$I_j = C_j I_{\mathrm{p}} + b(1 - C_j) I_{\mathrm{s}}, \quad (4)$$

where I_{p} is the local unpolarized profile within the photosphere, I_{s} that within the spot, and b the relative spot to photosphere brightness contrast. To compute I_{p}, we use the profile given by UR's analytical solution of the polarized radiative transfer equation in a Milne Eddington's atmosphere (see Hébrard et al. 2014 for the values of the different parameters) and we adjust the average line equivalent width to the observed value only. Following Dumusque et al. (2014), the local profile within the spot I_{s} is simply a broadened version (by a Gaussian of FWHM $w = 2$–3 km s^{-1}, depending on the stars) of that in the photosphere I_{p}. We also have the option of red shifting I_{s} with respect to I_{p} (to simulate the inhibition of the convective blue shift within the spot). However, we did not use this option for the present study given that convective blue shifts of M dwarfs are expected to be quite small.

As a result of their low $v \sin i$, our sample stars feature spectral lines that mostly reflect their intrinsic profiles rather than their Doppler broadening (as opposed with most stars studied to date with conventional Doppler imaging, e.g. Collier Cameron 1992; Morin et al. 2008a). The consequence is that a direct modelling of the observed profiles would critically depend on our ability to achieve a detailed description of the local profile.

To overcome this limitation, we propose a novel technique, based on interpreting the residuals with respect to the average profile, rather than the profiles themselves. Practically speaking, we start the process by computing the average profile over the whole data set $< I >$. We then subtract $< I >$ from each individual Stokes *I* profile of the time series to derive the profile residuals *RI* that directly reflect the profile distortions and include most information about the spot distribution to be reconstructed. In parallel, we model $< I >$ by adjusting the parameters of the local profile I_{p} until we obtain a good fit (including the Doppler broadening); we call this model average profile $< I' >$. We then sum the *RI* residuals to $< I' >$ and obtain a new data set I'. Since $< I' >$ is now perfectly known, the imaging code can concentrate its efforts on reproducing the *RI* residuals, i.e. the core material of our data set.

5.2 Simulations

We performed a set of simulations to test the performances of our novel reconstruction method. From an initial brightness map, we compute the associated Stokes *I* and *RI* data set for a given $v \sin i$, stellar inclination i, and spectral resolution. The objective is to retrieve both the brightness map and the quantities derived from the reconstructed profiles : the RV curve v_{r}, FWHM and v_{s}.

We present below the simulation results obtained in the case of slow rotators ($v \sin i \leq 4$ km s^{-1}), and derived assuming a spectral resolving power of 10^5 (*i.e.* the resolution of HARPS-Pol). We further assume that the S/N of the LSD profile residuals *RI* is equal to 4000 (value close to the observed S/N). Two different cases are studied: (i) a dense and regular sampling to test more specifically the use of the residuals (simulation A), and (ii) irregular sampling based on the observation of GJ 479, to mainly estimate the impact of a realistic phase coverage on the determination of the average profile (simulation B).

Dark spots are assumed to be circular with a relative size f[5] with respect to the overall stellar surface. The total equivalent spot area, ϵ, is thus defined as $\epsilon = f \times (1 - C) \times b$. For our simulation, we set $b = 0.5$. We consider two dark spots : spot #1 has a relative area of $f_1 = 3$ per cent with $C_1 = 0.4$ and thus $\epsilon_1 = 0.9$ per cent, and is located at 20° of latitude, spot #2 is characterized by $f_2 = 1.5$ per cent with $C_2 = 0.2$, and thus $\epsilon_2 = 0.6$ per cent, and is at 50° of latitude. The full equivalent spot area ϵ is equal to $\epsilon_1 + \epsilon_2 = 1.5$ per cent. The $v \sin i$ of the star ranges from 1 to 4 km s^{-1}, and the stellar inclination is $i = 60°$. The local profile within a spot is 15 per cent larger than in the quiet photosphere.

5.2.1 *Reconstructed map*

Fig. 8 (top part) and Table 8 show, respectively, the maps and their associated reconstructed characteristics. To test the impact of using the profile residuals *RI* instead of Stokes *I*, we compare the maps obtained using Stokes *I* profiles directly (called hereafter 'the

[5] Defined as the fractional area of the star covered by a spot, $\frac{1-\cos\alpha}{2}$, see Hébrard et al. (2014).

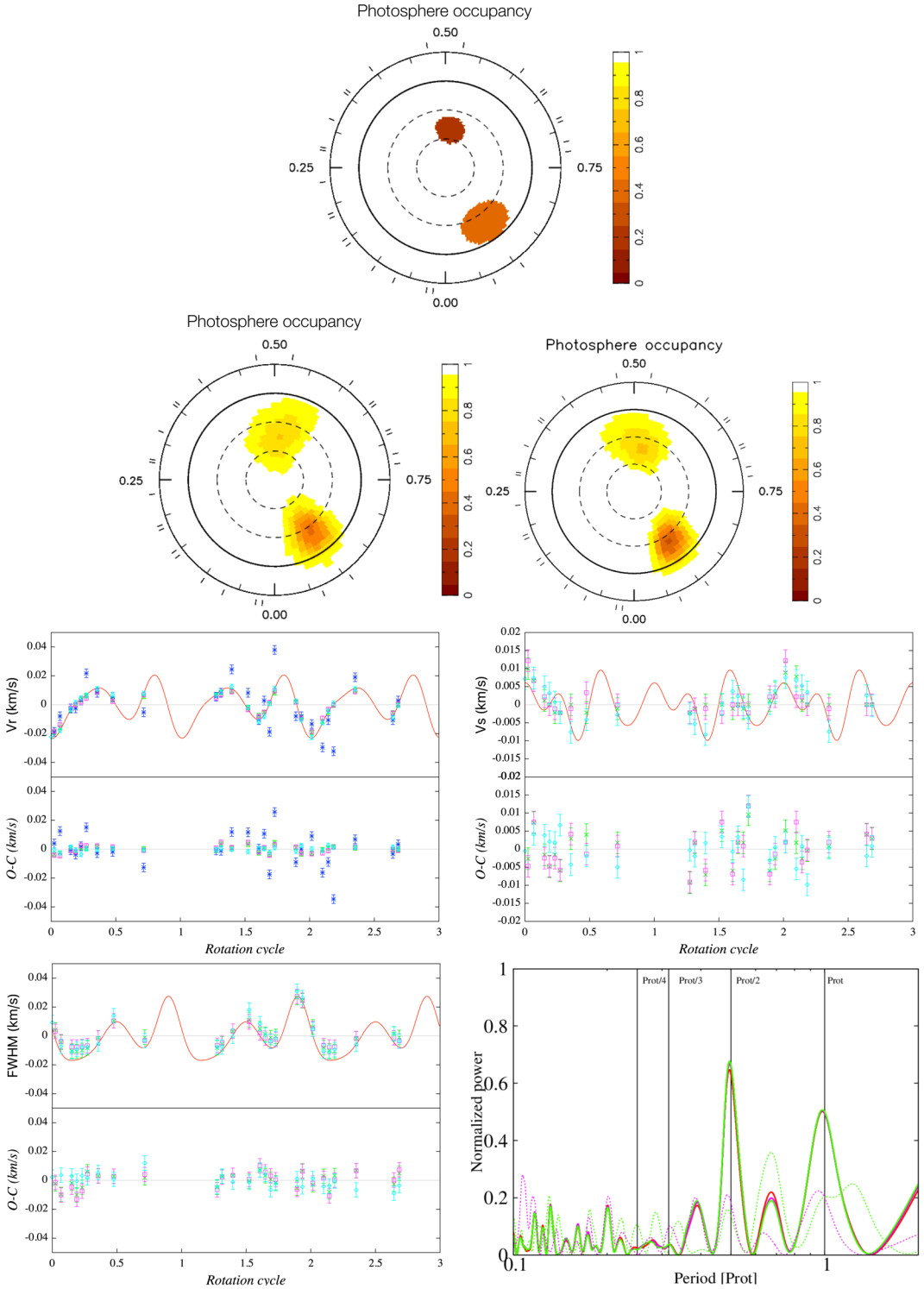

Figure 8. Reconstructed map obtained for a simulated star with $v \sin i = 1$ km s^{-1} and $i = 60^\circ$ featuring an equivalent spot area ϵ of 1.5 per cent. Top: spot distribution to reconstruct. Second row, left: reconstructed map from *I* with the realistic sampling B. Second row, right: same as left but reconstructed from *RI* residuals. The colour scale depicts the photosphere filling factor of each cell C_j (white corresponding to an unspotted cell). Third row, left: original v_r's (red solid line) compared with those reconstructed using either the conventional (pink open squares) or residual (green crosses) imaging method, respectively, and with those derived from the v_r versus v_s anticorrelation (blue asterisks). The multiple sine fit to the data (cyan open diamonds) is also shown. The corresponding O−C residuals are presented on the bottom curve. The grey line depicts the 0 m s^{-1} level. Third row, right: same as third row, left but for v_s. Bottom left: same as third row, left but for FWHM. Bottom right: periodograms of v_r (solid red line), of the v_r computed from data set obtained with the conventional method (solid pink line), and with the residual method (solid green line). The periodograms of the filtered RVs (using either the conventional or the residual method) are, respectively, shown with the red and green dashed lines. The vertical lines outline the rotation period (in unit of P_{rot}) and its 3 first harmonics ($P_{rot}/4$, $P_{rot}/3$, $P_{rot}/2$).

Table 8. Parameters of the reconstructed map for a star with $v \sin i$= 1 km s^{-1} and $i = 60^\circ$ with two spots covering 1.5 per cent of the stellar surface. Column 1 gives the considered simulations, and column 2 the $v \sin i$ of the stars. Columns 3 and 4 indicate the initial and final χ^2_r associated with the reconstruction. Column 5 gives the spotted reconstructed area. The results obtained from imaging using directly *I* are given in black, the results obtained from *RI* are given in blue. Simulation A: reconstruction from a dense and regular sampling. Simulation B: reconstruction from a random sampling.

Simu	$v \sin i$ (km s^{-1})	Initial χ^2_r	Final χ^2_r	Spotted area (%)
	Imaging from I = conventional method			
A	1	6.5	1.0	1.35
	2	12.2	1.0	1.45
	4	24.9	1.0	1.50
B	1	4.7	1.0	1.30
	2	8.1	1.0	1.45
	4	17.4	1.0	1.50
	Imaging from I' = residual method			
A	1	4.7	1.13	1.35
	2	11.5	1.11	1.40
	4	24.7	1.0	1.50
B	1	3.3	1.15	1.25
	2	8.2	1.1	1.40
	4	18.0	1.0	1.45

conventional method') with those obtained from the I' replacement data set described above (called below 'the residual method').

We note that the global spot distribution is recovered, whatever the technique we used. With the conventional method, $\chi^2_r = 1.0$ is reached whatever the $v \sin i$ and the phase coverage. However the spotted area is roughly underestimated with decreasing $v \sin i$. A similar but amplified behaviour is observed with the residual method. The use of the average profile $< I >$ to compute the I' data set mainly affects the reconstructed spotted equivalent spot coverage ϵ, which ends up being underestimated (1.25–1.45 per cent instead of 1.5 per cent depending on the $v \sin i$). This loss of accuracy when $v \sin i$ decreases mainly reflects that information gets increasingly blurred in longitude as stellar rotation slows down, thus weakening profile distortions and making them harder to reconstruct for the code.

5.2.2 *Model of the RV jitter*

The main parameter we aim at recovering is the RV curve shown in Fig. 8 (third row, on the left) in the case of $v \sin i = 1$ km s^{-1}.

First, we note that RV variations are fitted down to the noise level, with both methods. For this spot configuration, the periodogram exhibits conspicuous peaks at $P_{\rm rot}$ and $P_{\rm rot}/2$. We find that both imaging methods provide similar results in the sense that they are quite successful at filtering the rotationally modulated activity jitter; we do not observe any strong peaks in the periodogram of the RV residuals O−C (= observed - computed, see periodograms Fig. 8, bottom-right panel).

To quantify the model efficiency, we compare the rms of O−C data (see Table 9) using the two different imaging methods (based on *I* and I') with that derived from the multiple sine fits of $v_{\rm r}$ (with fundamental + 1 to 3 harmonics), and from the usual anticorrelation observed between $v_{\rm s}$ and $v_{\rm r}$ (e.g. see Melo et al. 2007, for more details). From these results, we clearly see that the quality of the filtering based on Doppler imaging is similar to the one obtained from the multiple sine-fit (fundamental + 2 first harmonics), and much better than that based on the anticorrelation between $v_{\rm s}$ and $v_{\rm r}$. More specifically and with respect to the latter case, we decrease the rms dispersion by a factor of 5 to 8 (depending on the $v \sin i$).

Table 9. Column 1 gives the studied simulation, column 2 the $v \sin i$ of the star. Column 3 indicates the rms RV noise, whose increase with $v \sin i$ reflects the decrease in RV precision resulting from the shallower and broader line profiles of faster rotators. Columns 4–9 give the rms of the RV residual, after a filtering from the direct method (b), from the indirect method (c), from a multiple sine-fit with, respectively, 1, 2 and 3 harmonics (d)–(f), and from the anticorrelation $v_{\rm r}$−$v_{\rm s}$ (g).

Simu	$v \sin i$ (km s^{-1})	(a)	(b)	(c)	(d)	(e)	(f)	(g)
		(m s^{-1})						
A	1	1.5	2.0	2.4	4.9	1.6	1.5	12.9
	2	1.7	2.4	2.4	10.4	2.1	1.5	11.9
	4	2.9	3.2	3.2	25.3	6.3	2.8	27.3
B	1	1.6	1.8	2.1	3.6	1.7	1.4	17.7
	2	1.8	1.8	2.1	8.3	2.0	1.2	13.4
	4	3.2	3.2	3.3	18.5	4.6	2.6	31.3

The use of the profile residuals *RI* can lead to a small underestimate of the equivalent spot area epsilon (for smaller values of $v \sin i$ in particular); however, the RV filtering is not affected reaching down to almost the noise level with both methods.

Finally, the density of the sampling does not affect much the quality of the reconstructed RVs, as long as it is dense and even enough (typically a few tens of observing points covering a few rotation cycles). The lowest the $v \sin i$, the stronger the importance of the sampling.

5.3 Application to M dwarfs

We apply the residual imaging method presented and tested in Sections 5.1 and 5.2 to recover the parent spot distribution generating the observed RV activity jitter for the various stars of our sample.

To assess the likelihood of the RV fit we obtain from the map, we compute the FAP as presented in Section 4.2.2. We take the multiple sine fit of $v_{\rm r}$ (fundamental + 2 first harmonics) as a reference to compute $\Delta\chi^2$; we then obtain (with a formula resembling equation 3):

$$\Delta\chi^2 = \frac{\chi^2_{r,0} - \chi^2_{r,2}}{\chi^2_{r,1}} N \quad (5)$$

with $\chi^2_{r,1}$ and $\chi^2_{r,2}$, respectively, corresponding to the χ^2_r of the multiple sine fit and of the fit obtained with the Doppler imaging based on residual reconstruction (hereafter DI fit). The number of degrees of freedom associated with the imaging process is estimated from the number of parameters associated with the non-axisymmetric SH modes needed to describe the observed variations, i.e. ∼20 for $l \leq 4$. Results are presented in Table 6.

5.3.1 *GJ 358*

From the *RI* profiles (see Fig. 9), we reconstruct the map shown in Fig. 10, featuring an equivalent spot coverage ϵ of ∼1 per cent (with $b = 0.5$). The initial χ^2_r is 3.8 and corresponds to the fit to the *RI* spectra with an unspotted star. Adding spots on the stellar surface allows the code to reduce χ^2_r down to 2.1, with a main spot at high latitude (∼60°), and extending towards the equator.

Synthetic RV curve derived from this brightness map exhibits a full amplitude of 8.5 m s^{-1}, and matches the data down to

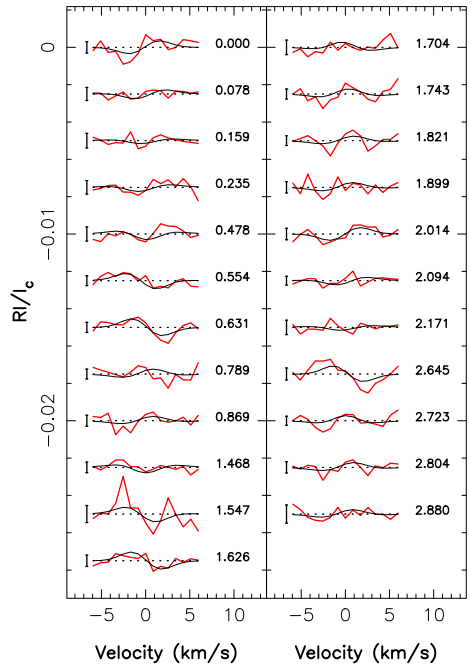

Figure 9. Temporal series of *RI* of GJ 358. Data are in red, the modelled *RI* are in black. On the right of each spectrum, we indicate the observation phase, on the left the 1σ error bars.

$\chi^2_{r,2} = 2.05$. The rms of the RV residuals is 2.88 m s^{-1} (whereas $\sigma_0 = 2.08$ m s^{-1}). The low FAP (<0.01 per cent) demonstrates that the imaging process provides a very significant improvement in the quality of the fit to the data. Moreover, in the v_r periodograms we clearly see that (i) the signals at $P_{\rm rot}$, $P_{\rm rot}/2$ and $P_{\rm rot}/3$ have been removed, and (ii) no major periodic signal remains.

5.3.2 GJ 479

The reconstructed spots have an equivalent surface of ∼1.4 per cent, and are located at mid-latitude (∼ 40°, see Fig. H1). It corresponds to a final χ^2_r of 2.9 (starting from $\chi^2_r = 5.0$).

The $J_{\rm m}$ component of the RV jitter deduced from this map has a peak-to-peak amplitude of 11 m s^{-1}, and the rms of RV residuals is 3.93 m s^{-1}. Once $J_{\rm m}$ is subtracted from RV data, the periodogram does not exhibit any strong peak anymore: the filtering allows us to clean up the signals whose periods are $P_{\rm rot}$, $P_{\rm rot}/2$, $P_{\rm rot}/3$.

5.3.3 GJ 410

For GJ 410, we collected observations over three months (*i.e.* six stellar rotations). We note that all the *RI* spectra do not identically repeat from one rotation cycle to the next (see e.g. phases 2.7 and 3.7, or phases 4.9 and 5.9 in Fig. 11). For this star, one of the most active of the studied sample, we first carried out a reconstruction for the whole data set (see Fig. H2). In a second step, we divided the data set into three sequential subsets to take into account the evolution of spot coverage on the stellar surface, respectively, corresponding to rotation cycles 1.928–2.707 (epoch #1, 9 observations), 3.777–4.988 (epoch #2, 12 obs) and 5.058–6.199 (epoch #3, 7 obs). The results are given in Fig. 12.

Dividing the data into multiple subsets allows us to improve the fit to the data, with a final χ^2_r decreased from 2.0 (for the complete set) to 1.2–1.7 (for the individual subsets), as shown Table 10. The reconstructed maps show that in epoch #1 a main dark spot at low latitude around phase 0.6 is visible at the stellar surface, with a fainter spot at phase 0.25 and 30° of latitude. This secondary spot grows and strengthens in epochs #2 and #3, and a new spot appears at phase 0.95 from epoch #2 onwards.

Moreover, the quality of the RV filtering increases within each of our subsets. The modelled RV curves we derive match the observed ones at a χ^2_r level of 1.0–1.9, to be compared with 4.1 when processing the whole data set (see Table 10). We conclude that in the case of GJ 410, the main variability observed in RV data likely comes from short-lived spots, inducing an evolution in the shape of the RV curve on a time-scale of only two rotation cycles.

5.3.4 GJ 205

For GJ 205, the amplitude of the *RI* spectra is low (≤0.05 per cent, see Fig. G1). The DI reconstruction leads to an equivalent spotted area ϵ of ∼0.9 per cent that allows us to decrease the χ^2_r fit to the profiles from 4.3 to 3.8 only. The reconstructed features exhibit faint spot clusters, located at high and mid-latitude, however, this reconstruction is not reliable given the FAP of 75 per cent associated with the Stokes *I* LSD fit. The RV jitter is not efficiently filtered (FAP ∼ 98 per cent). These results validate that there is likely no signals at $P_{\rm rot}$ and that DR might strongly affect the dark spot location at the surface of GJ 205 and thus the RV activity jitter of the star. Further work, taking explicitly into account DR, is thus needed for this star. This would require in particular a high-quality spectropolarimetric data set from which DR can be reliably estimated.

5.3.5 Discussion

The efficiency of the RV filtering depends on the relative importance of the rotationally modulated RV component with respect to the random component. The importance of each component is reminded in Table 11.

For the lowest mass star of this sample, GJ 358, the rotational modulated component $J_{\rm m}$ of the RV jitter have been divided by 2.8 (and $J_{\rm tot}$ by 2.2). For the earliest M dwarfs (GJ 205 and GJ 410), neither the DI modelling nor the multiple sine fit succeed at obtaining a decent match to the observed RV jitter (high FAP), because of a higher level of intrinsic variability of the RV curve. In the particular case of GJ410, we observe that this higher level of intrinsic variability is directly related to the short spot lifetimes (1–2 rotation cycles), as evidenced by the significant improvement in the efficiency of the DI filtering when considering shorter time intervals (see Table 11). Contrary to a simple multiple sine fit, the use of the imaging techniques allows one to (i) to better constrain the origin of the activity jitter (dark spots and rotational modulation, DR or short spot lifetime), and (ii) to obtain a self-consistent physically motivated, though still simple, description of the activity jitter rather than to perform a blind filtering of the RV data.

Our model is based on the assumption that the dominant contribution to the total RV signal in the M dwarfs should be the effect of dark spots. This assumption mainly relies on Sun-like stars studies, and on the low temperature of M dwarfs. However, we have to note that the current DI model does not yet allow us to faithfully reproduce the full amplitude of FWHM of the four studied stars. The phase of the variations are fitted, but the peak-to-peak amplitude is always underestimated in each case. This caveat may reflect inadequate assumptions/approximations in our modelling and will

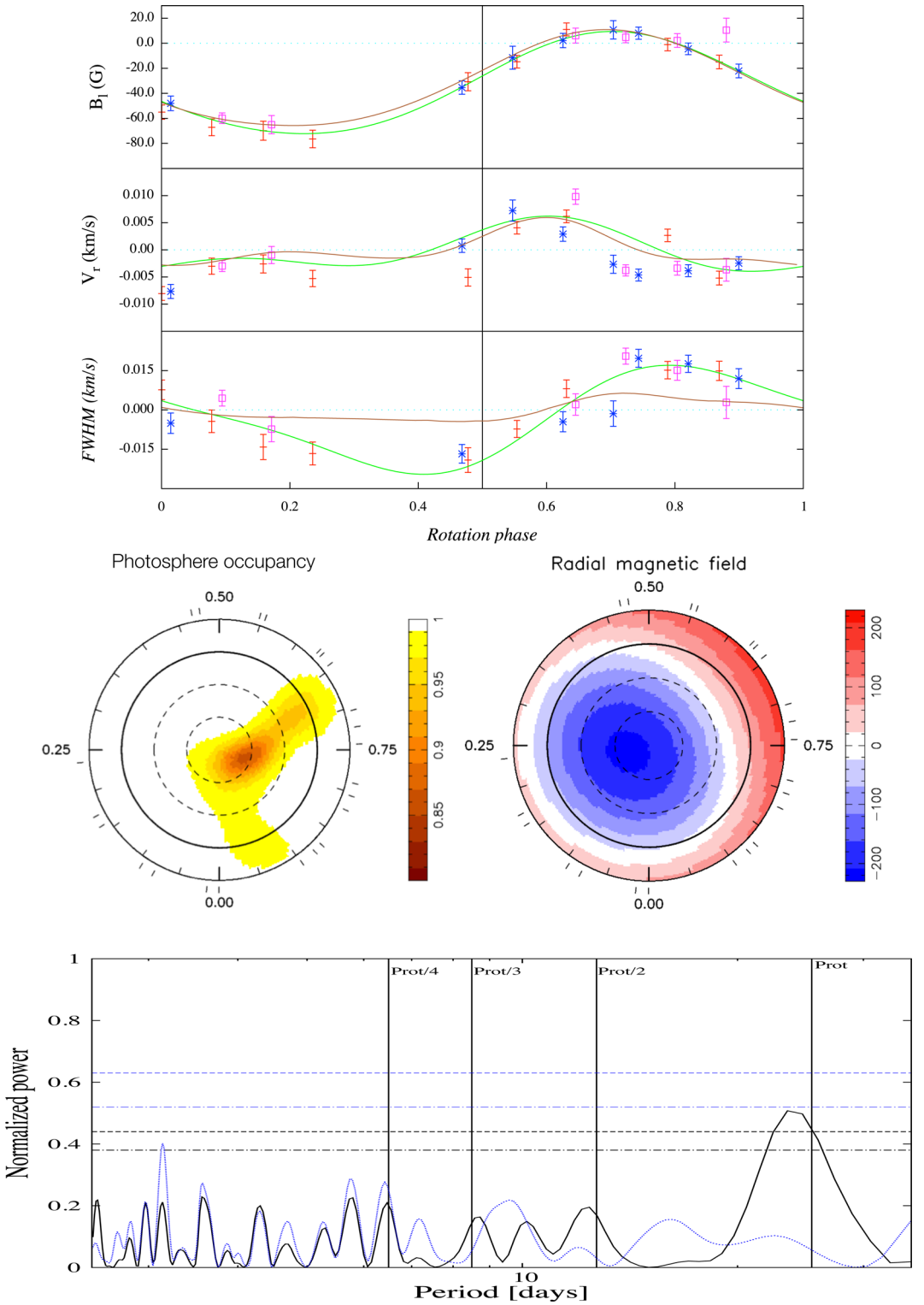

Figure 10. Top: temporal evolution of B_l, v_r and FWHM (with respect to the average value) of GJ 358. Data and their error bars are represented in red, blue and pink according the rotation cycle (cycle 1 in red, cycle 2 in blue and cycle 3 in pink). The green curves corresponds to the sine fit, and the brown curves represents the RVs computed from the DI map. Middle left: maps of the filling factor of the photosphere (white means that there is only quiet photosphere, brown means there is only spot in the cell), and Middle right: map of the radial large-scale magnetic field. Bottom: periodograms of observed RVs (black), and of the RVs after the RV filtering from DI (blue). The FAP at 1 and 10 per cent are represented in dotted lines and dot–dashed lines.

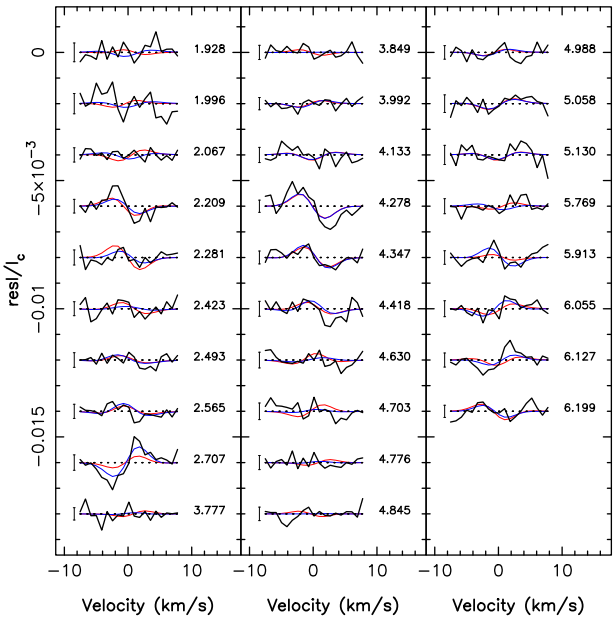

Figure 11. As Fig. 9, for GJ 410. The blue fit represents the fit from epochs #1 to #3, the red fit represents the fit from the full data set.

be further explored in forthcoming papers. The next step will be to add more physical realism in our model (e.g. use a more realistic line profile I_s to characterize the spotted regions) to improve the modelling of the effects of the activity jitter in M dwarfs.

Table 11. Same as Table 7, with three additional columns: column 5 gives J_m, the rms of the RV data modelled using the DI imaging, column 7 gives A_2, quantifying how we can reduce the activity jitter thanks to DI imaging, and column 8 gives $A_3 = J_m / \sqrt{J_m^2 - J_{m,DI}^2}$, denoting the factor of decrease of the J_m component. The dash indicates that data can be reproduced down to the noise level, i.e. that the RV variations are due to rotational modulations only.

	J_{tot}	J_m (m s^{-1})	J_r	J_m with DI	A_1	A_2	A_3
GJ 205	3.21	1.75	2.68	1.53	1.2	1.1	2.1
GJ 410	8.21	5.67	5.93	5.82	1.4	1.3	3.1
epoch #1	9.01	9.01	–	8.43	–	3.8	3.9
epoch #2	6.37	6.02	2.07	5.95	3.1	2.8	6.6
epoch #3	5.10	5.10	–	5.04	–	5.2	6.5
GJ 479	4.89	3.83	3.04	3.54	1.7	1.5	2.6
GJ 358	4.31	4.10	1.33	3.83	3.2	2.2	2.8

6 SUMMARY AND PERSPECTIVES

The magnetic analysis gives access to the large-scale magnetic field map of the observed weakly active M dwarfs, as well as to a reliable and accurate estimate of P_{rot}. Fig. 13 summarizes the magnetic properties of our sample. These data allow us to add new observations in the $M_\star - P_{rot}$ diagram, covering a mostly unexplored domain so far. The magnetic fields detected for the early-M dwarfs exhibit strengths of a few tens of G, and are lower by a factor of 5 than those of more active and rapidly rotating mid-M dwarfs (Morin et al. 2008b). We note that for the stars with a stellar mass larger

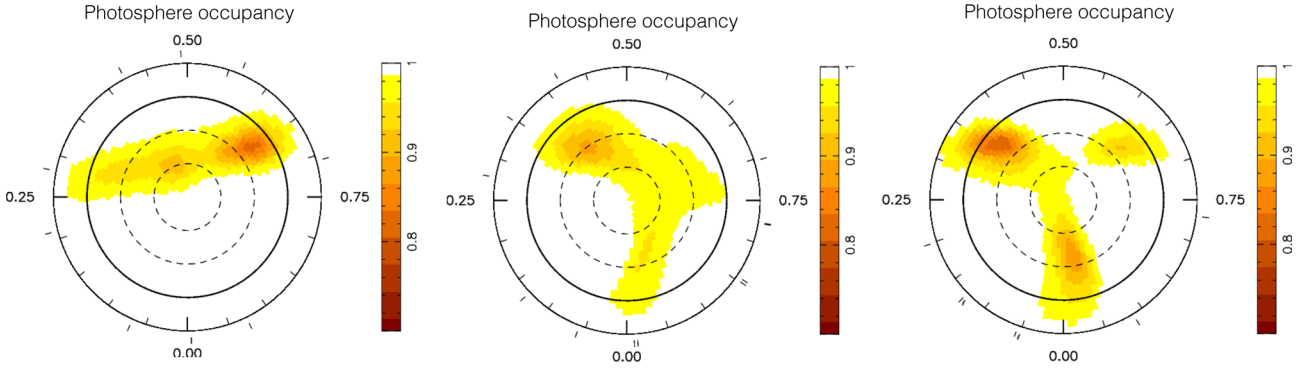

Figure 12. Maps of the filling factor of the photosphere of GJ 410 (white means that there is only quiet photosphere, brown means there is only spot in the cell) at the three epochs [from (1) to (3), from left to right].

Table 10. Same as Table 6 for the three observation epochs of GJ 410. For the observation epochs (1) and (3) a single harmonics is sufficient to reach residual RVs lower than 3 m s^{-1}. The RV jitter can by entirely modelled with rotational modulation ($rms_{J,r} \sim 0$m s^{-1}, et $rms_{J,tot} \sim rms_{J,m}$), and we choose $\chi^2_{r,1} = 1.0$ and $rms_1 = \sigma_0$.

	Raw RV data			Multiple sine-fit (fund. + 1 or 2 harm.)			DI modelling					
							RV curves			LSD profiles		
	σ_0 (m s^{-1})	rms_0 (m s^{-1})	$\chi^2_{r,0}$	rms_1 (m s^{-1})	$\chi^2_{r,1}$	FAP (%)	rms_2 (m s^{-1})	$\chi^2_{r,2}$	FAP (%)	$\chi^2_{r,i}$	$\chi^2_{r,f}$	FAP (%)
epoch #1	3.43	9.64	8.40	3.43	1.0	≤0.01	4.67	1.92	≤0.01	2.8	1.7	≤0.01
epoch #2	3.22	7.14	6.29	3.83	1.03	≤0.01	3.95	1.66	≤0.01	2.5	1.6	≤0.01
epoch #3	3.06	5.94	3.91	3.06	1.0	≤0.01	3.19	1.02	17	2.2	1.2	≤0.01
full set	3.28	8.84	7.85	6.55	3.96	0.04	6.78	4.14	2.8	2.9	2.0	≤0.01

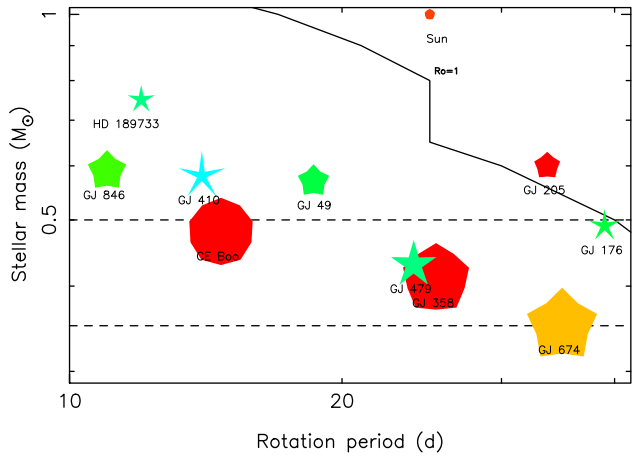

Figure 13. Properties of the magnetic topologies of our sample of five M dwarfs as a function of rotation period and stellar mass. Larger symbols indicate larger magnetic fields, while symbol shapes depict the different degrees of axisymmetry of the reconstructed magnetic field (from decagons for purely axisymmetric fields to sharp stars for purely non-axisymmetric fields). Colours illustrate the field configuration (dark blue for purely toroidal fields, dark red for purely poloidal fields and intermediate colours for intermediate configurations). The solid line represents the contour of constant Rossby number $R_o = 1$. The dotted line correspond to the 0.5 and 0.35 $M_\odot$ thresholds. The Sun, GJ 49 and CE Boo (Donati et al. 2008), HD 189733 (Fares et al. 2010) and GJ 674 and GJ 176 presented in detail in a forthcoming paper are shown for comparison.

than 0.5 $M_\odot$, the toroidal component is significant, except for GJ 205 whose large-scale magnetic field is dominated by a poloidal component. GJ 205 is the only observed star with a Rossby number R_o[6] higher than 1 (as the Sun). This is in agreement with the trends previously reported in Donati & Landstreet (2009), where stars with $R_o > 1$ tend to exhibit weak poloidal fields mostly aligned with the rotation axis.

For $M_\star < 0.5$ $M_\odot$, the large-scale magnetic properties are diverse, with some stars featuring mainly poloidal and axisymmetric fields (GJ 358, GJ 674) and some others exhibiting more complex topologies (GJ 479, GJ 176). In particular, we note that two stars of our sample feature different types of fields while sharing the same location in the $M_\star$ versus P_{rot} plane. This is reminiscent of the bistable behaviour of dynamo processes, as previously pointed out by, e.g. Morin et al. (2011) in the case of active very low mass dwarfs. The theoretical models (e.g. Gastine et al. 2013) foresee a bistability around $R_o = 0.1$, with a transition between fields with a simple dipolar topology ($R_o < 0.1$) and fields with a complex topology ($R_o > 1$). Our observations suggest that dynamo bistability may indeed be present at different places of the $M_\star$ versus P_{rot} diagram than previously identified by Morin et al. (2011) and whose relation with theoretical predictions is yet to be checked in more details. More spectropolarimetric observations of M dwarfs in this range of mass and rotation periods are necessary to investigate this result in more details.

To find an Earth-like planet (in terms of size, mass and effective stellar flux) thanks to the RV method, moderately active M dwarfs appear to be natural targets with their reduced effective temperature and their low mass. However, we still need to model and filter out the RV activity jitter to reveal these plausible low-mass planets RV signatures. To characterize the activity jitter of cool low-mass stars, we used the studies done for Sun-like stars (e.g. Dumusque et al. 2014), taking into account their reduced photospheric temperature. We then assumed the dominant contributor to the activity-modulated RV signal that plagues RV data is the rotational modulation caused by dark spot at the stellar surface (in agreement with theoretical studies as Beeck et al. 2015). With this hypothesis, we were able to develop a technique, based on a tomographic imaging (ZDI), to model the spot distribution at the surface of the four weakly active early-M dwarfs we observed.

The sampled stars being slow rotators ($v \sin i \leq 2$ km s^{-1}), the observed spectral line width reflects directly intrinsic profiles rather than the Doppler broadening. To overcome this issue, we adapted the Doppler Imaging technique to reconstruct the profile residuals instead of the observed profiles themselves (see Section 5.1). Thanks to this approach, we are not dependent anymore on our ability at achieving a detailed description of the local profile, and the code is focused on the profile distortion modelling only. Besides, this method relies on the knowledge of the rotational period P_{rot}, parameter previously estimated from the magnetic analysis.

The novel imaging method we devised is found to be reasonably successful at reconstructing the spot distribution at the surface of the early-type slowly rotating stars that we studied. From this map and its associated set of spectra, we model the RV activity jitter whose period is commensurate to P_{rot}, i.e. J_m component only. For our early-M dwarf sample, we found that the spots cover up to 2 per cent of the total stellar surface (in agreement with previous estimates for rapid rotators, see e.g. Morin et al. 2008a). The rotationally modulated RV component deduced from the brightness maps allows us to reduce the observed RV jitter by a factor of 2–3, and the observed rotationally modulated component by a factor of 3–6. The efficiency increases with decreasing stellar mass. For the earliest M dwarfs, we speculate that the high level of intrinsic variability likely caused by short-lived spots having lifetimes of < 2 rotation cycles limits the efficiency of the modelling. A modelling of such effect is possible but requests specific observational strategy, with a high cadency sampling during more than three rotational cycles. Although relying on a simple assumption, this method gives promising results, and allows us to get a better insight on the origin of the activity RV jitter of early-M dwarfs. This study of slowly rotating early-M dwarfs complements the analysis already done for late-M dwarfs (e.g. Barnes et al. 2011, 2014, 2015).

To investigate if spot distributions relate to large-scale magnetic field topologies, we compare both the brightness and magnetic field maps that we obtained (see Fig. 14). It seems that the darkest spots concentrate either close to the magnetic poles (GJ 358 whose magnetic field is mainly poloidal), or to the magnetic equator (GJ 410 and GJ 479 whose magnetic field is significantly toroidal) – we exclude GJ 205 in this study, given the weak reliability of the spot distribution map. This suggests that the large-scale magnetic field may indeed be controlling where surface spots tend to preferentially appear at the stellar surface, as it does in the particular case of the Sun. This tendency needs to be examined in a larger sample with new spectropolarimetric surveys of moderately active M dwarfs. Besides, given that surface spot distributions are significantly impacting our ability at detecting Earth-like planets (see e.g. simulations done by Andersen & Korhonen 2015), it will be worthwhile to extent this study to later-type M dwarfs to improve our knowledge of their spot patterns. For example, the Doppler imaging is a powerful tool to investigate whether spot patterns change and, e.g. evolve towards more even distributions

[6] R_o is defined as $R_o = P_{rot}/\tau_c$, where τ_c is the convective turnover time derived by Kiraga & Stepien (2007) from the rotation-activity relation in X-rays.

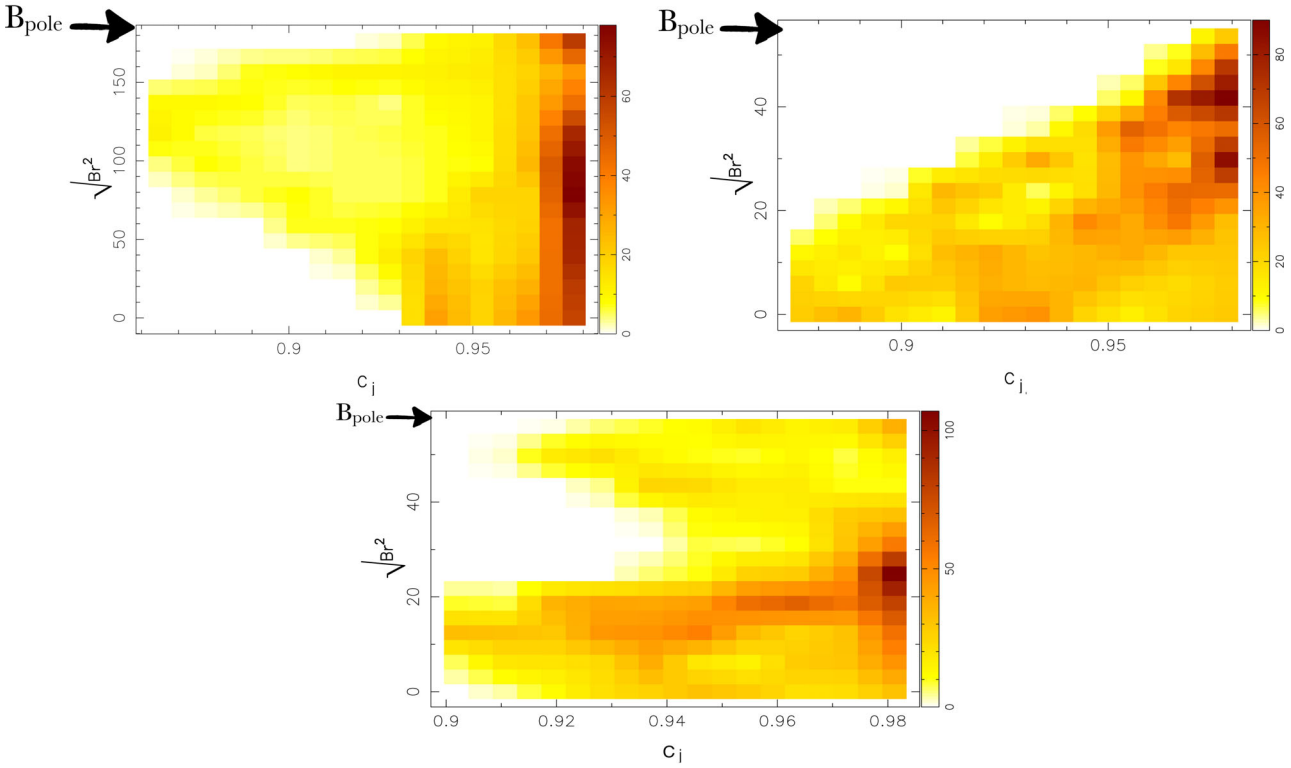

Figure 14. The *x*-axis depicts the C_j, denoting the proportion of photosphere inside each cell, and the *y*-axis the absolute value of the radial component of the large-scale magnetic field. The colour scale represents the number of cells affected by both a radial magnetic field and a dark spot. The arrow indicates the absolute value of the radial polar magnetic field of the star. Top left: GJ 358. Top right: GJ 479. Bottom: GJ 410.

of smaller features, when going from partially to fully convective stars.

Further improvements can be implemented to obtain a more accurate filtering of the RV curves of M dwarfs (e.g. by incorporating the temporal evolution of spots within the imaging process). Moreover, adapting our method to stars of other spectral types (G and K), for which the activity jitter is no longer dominated by the spot brightness contrast but by plages and the suppression of convective blueshift (e.g. Haywood et al. 2014), is another obvious avenue worth exploring. Finally, a complementary study is in preparation to present the performances of this technique for M dwarfs hosting a planet.

To disentangle stellar from planetary signals, a powerful analysis should be to carry out observations at both optical and IR wavelengths, particularly for M dwarfs emitting a large fraction of their flux in the IR. Several studies showed that the RV jitter will be divided by at least a factor of 2 due to the lower contrast between the dark spot regions and the quiet photosphere (Marchwinski et al. (2015) and Reiners et al. (2010), Rodler et al. (2011), respectively, for Sun-like stars and late-M dwarfs). In this context, the new generation of high resolution/precision velocimeters working in the nIR domain (e.g. CARMENES[7], SPIRou[8], CRIRES+[9]) present a tremendous interest. However, characterizing, modelling and filtering out the RV activity jitter of M dwarfs remain mandatory steps for all future velocimetric studies aiming at detecting small Earth-mass rocky planets. They allow us to define the best adapted observational strategies, taking into account the specificities of the M dwarf activity that hampers RV measurements. Moreover, while the brightness contrast decreases in the IR, the impact of small-scale magnetic field on RVs strengthens through Zeeman effect. Therefore, the method we presented will be particularly adapted for SPIRou, which will be both a high-precision velocimeter and a spectropolarimeter. Spectropolarimetric surveys in nIR will give new options for filtering RV curves from the activity jitter using tomographic techniques like ZDI, and will efficiently further enhance the sensitivity to low-mass planets, as well as to the magnetic stellar activity RV signal itself.

[7] Calar Alto high-Resolution search for M dwarfs with Exoearths with Near-infrared and optical Echelle Spectrographs, a high-precision velocimeter at the 3.5 m telescope at the Calar Alto Observatory.

[8] SpectroPolarimeter in the near InfraRed, a spectropolarimeter/high-precision velocimeter for the 3.6 m Canada–France–Hawaii Telescope. It will operate at near-infrared wavelengths (first light in 2017).

[9] Upgrade of the CRyogenic InfraRed Echelle Spectrograph at ESO/VLT (first light in 2018).

ACKNOWLEDGEMENTS

This paper is based on observations obtained at the 3.6 m telescope in La Silla, Chile, operated by ESO, the European Southern Observatory. We thank the La Silla staff for their valuable help throughout our observing runs and F. Bouchy for his help in the coordination of observing runs. We also thank the TBL staff for their help during data collection of GJ 410, GJ 205 and GJ 846. Finally, we thank X. Bonfils for his M mask that we used to compute RVs. JM was sponsored by a postdoctoral fellowship of the Alexander von Humboldt foundation in Göttingen. We acknowledge the PNPS/INSU (Programme national de Physique Stellaire) to fund this project. XD acknowledges funding from the LabEx OSUG@2020. Finally, thank you to the anonymous referee for the useful comments.

REFERENCES

Aigrain S., Pont F., Zucker S., 2012, MNRAS, 419, 3147
Andersen J. M., Korhonen H., 2015, MNRAS, 448, 3053
Baraffe I., Homeier D., Allard F., Chabrier G., 2015, A&A, 577, A42
Barnes J., Jeffers S., Jones H., 2011, MNRAS, 412, 1599
Barnes J. R. et al., 2014, MNRAS, 439, 3094
Barnes J. R., Jeffers S. V., Jones H. R. A., Pavlenko Y. V., Jenkins J. S., Haswell C. A., Lohr M. E., 2015, ApJ, 812, 42
Beeck B., Schüssler M., Cameron R. H., Reiners A., 2015, A&A, 581, A42
Boisse I. et al., 2009, A&A, 495, 959
Boisse I., Bouchy F., Hébrard G., Bonfils X., Santos N., Vauclair S., 2011, A&A, 528
Bonfils X. et al., 2007, A&A, 474, 293
Bonfils X., Gillon M., Udry S., Armstrong D., Bouchy F., 2012, A&A, 546, A27
Bonfils X., Delfosse X., Udry S., Forveille T., Mayor M., Perrier C., Bouchy F., 2013, A&A, 549, A109
Borgniet S., Meunier N., Lagrange A.-M., 2015, A&A, 581, A133
Brown S. F., Donati J.-F., Rees D. E., Semel M., 1991, A&A, 250, 463
Collier Cameron A., 1992, in Byrne P. B., Mullan D. J., eds, Lecture Notes in Physics, Vol. 397, Surface Inhomogeneities on Late-Type Stars. Springer-Verlag, Berlin, p. 33
Delfosse X., Forveille T., Ségransan D., Beuzit J.-L., Udry S., Perrier C., Mayor M., 2000, A&A, 364, 217
Desort M., Lagrange A., Galland F., Udry S., Mayor M., 2007, A&A, 473, 983
Donati J.-F., 2001, in Boffin H. M. J., Steeghs D., Cuypers J., eds, Lecture Notes in Physics, Vol. 573, Astrotomography, Indirect Imaging Methods in Observational Astronomy. Springer-Verlag, Berlin, p. 207
Donati J.-F., 2003, ASP Conf. Proc. Vol. 307, ESPaDOnS: An Echelle SpectroPolarimetric Device for the Observation of Stars at CFHT, p. 41
Donati J.-F., Landstreet J. D., 2009, ARA&A, 47, 333
Donati J.-F., Semel M., Carter B. D., Rees D. E., Collier Cameron A., 1997, MNRAS, 291, 658
Donati J.-F., Collier Cameron A., Petit P., 2003, MNRAS, 345, 1187
Donati J.-F., Forveille T., Cameron A. C., Barnes J. R., Delfosse X., Jardine M. M., Valenti J. A., 2006a, Science, 311, 633
Donati J.-F. et al., 2006b, MNRAS, 370, 629
Donati J.-F. et al., 2008, MNRAS, 390, 545
Dressing C. D., Charbonneau D., 2015, ApJ, 807, 45
Dumusque X., Boisse I., Santos N., 2014, ApJ, 796
Fares R. et al., 2010, MNRAS, 406, 409
Forveille T. et al., 2009, A&A, 493, 645
Gastine T., Morin J., Duarte L., Reiners A., Christensen U. R., Wicht J., 2013, A&A, 549, L5
Gomes Da Silva J., Santos N., Bonfils X., Delfosse X., 2011, A&A, 534, A30
Gray D. F., 1982, ApJ, 255, 200
Haywood R. et al., 2014, MNRAS, 443, 2517
Hébrard E., Donati J., Delfosse X., Morin J., Boisse I., 2014, MNRAS, 443, 2899
Kasting J. F., Kopparapu R., Ramirez R. M., Harman C. E., 2014, Proc. Natl. Acad. Sci., 111, 12641
Kiraga M., Stepien K., 2007, Acta Astron., 57, 149
Koen C., Kilkenny F., van Wyk F., Marang F., 2010, MNRAS, 403, 1949
Kurucz R., 1993, CDROM # 13, ATLAS9 Atmospheric Models and # 18 ATLAS9 and SYNTHE Routines, Spectral Line Database. Smithsonian Astrophysical Observatory, Washington DC
Leggett S., Allard F., Geballe T., Hauschild P., Schweitzer A., 2001, ApJ, 548, 908
Lomb N. R., 1976, Ap&SS, 39, 447
Marchwinski R. C., Mahadevan S., Robertson P., Ramsey L., Harder J., 2015, ApJ, 798, 63
Mayor M. et al., 2003, The Messenger, 114, 20
Melo C. et al., 2007, A&A, 467, 721
Meunier N., Desort M., Lagrange A.-M., 2010, A&A, 512, A39
Morin J. et al., 2008a, MNRAS, 384, 77
Morin J. et al., 2008b, MNRAS, 390, 567
Morin J., Donati J., Petit P., Delfosse X., Forveille T., Jardine M. M., 2010, MNRAS, 407, 2269
Morin J., Dormy E., Schrinner M., Donati J.-F., 2011, MNRAS, 418, L133
Moutou C. et al., 2007, A&A, 473, 651
Queloz D., Henry G., Sivan J., Baliunas S., Beuzit J., Donahue R., 2001, A&A, 379
Reiners A., Bean J., Hubert K., Dreizler S., Seifahrt A., 2010, ApJ, 710, 432
Robertson P., Mahadevan S., Endl M., Roy A., 2014, Science, 345, 440
Rodler F., Del Burgo C., Witte S., Helling C., Hauschildt P. H., Martín E. L., Álvarez C., Deshpande R., 2011, A&A, 532, A31
Scargle J. D., 1982, ApJ, 263, 835
Snik F., Kochukhov O., Piskunov N., 2011, in Kuhn J. R., Harrington D. M., Lin H., Berdyugina S. V., Trujillo-Bueno J., Keil S. L., Rimmele T., eds, ASP Conf. Ser. Vol. 437, Solar Polarization 6. Astron. Soc. Pac., San Francisco, p. 237
Zechmeister M., Kürster M., 2009, A&A, 496, 577

APPENDIX A: ROTATION PERIODS DERIVED FROM B_l, RV, FWHM AND Hα

Table A1. Rotation periods derived from B_l, RV, FWHM and Hα measurements and the estimated error bars at 1σ for the four stars of the sample.

Star	$P_{\rm rot}^{B_l}$ (d)	$P_{\rm rot}^{\rm RV}$ (d)	$P_{\rm rot}^{\rm FWHM}$ (d)	$P_{\rm rot}^{\rm H\,\alpha}$ (d)
GJ 205	33.63 ± 0.37	39.70 ± 0.85	41.9 ± 1.9	33.46 ± 0.80
GJ 410	13.83 ± 0.10	14.20 ± 0.10	14.76 ± 0.20	15.15 ± 0.30
GJ 479	24.04 ± 0.75	23.2 ± 1.9	25.48 ± 0.81	22.94 ± 0.60
GJ 358	25.37 ± 0.32	24.47 ± 0.60	25.49 ± 0.42	23.8 ± 2.7

APPENDIX B: OBSERVATIONS JOURNAL

Observations journal for the four M dwarfs observed from 2013 October to 2014 August with HARPS-Pol@LaSilla and NARVAL@TBL.

Table B1. Journal of observations for GJ 479. Columns 1–5, respectively, list, the rotational cycle (computed with the rotation period mentioned in Table 1 according to ephemeris given by equation 1), the date of the beginning of the night, the BJD, the observation site, the peak S/N (per 0.85 km s^{-1} velocity bin). Columns 6 and 7 give, respectively, B_l and RV values.

Cycle	Date	BJD (+2456000)	Instrument	S/N	B (G)	RV (km s^{-1})
0.024	14 apr 30	778.5870	HARPS-Pol	133	20.54 ± 7.03	8.17e-03 ± 1.56e-03
0.069	14 may 01	779.6500	HARPS-Pol	121	3.36 ± 7.82	4.08e-03 ± 1.74e-03
0.151	14 may 03	781.6390	HARPS-Pol	108	8.61 ± 9.02	5.16e-03 ± 1.97e-03
0.190	14 may 04	782.5590	HARPS-Pol	135	5.46 ± 7.04	5.53e-03 ± 1.43e-03
0.231	14 may 05	783.5600	HARPS-Pol	102	24.94 ± 9.97	−6.72e-03 ± 2.09e-03
0.272	14 may 06	784.5480	HARPS-Pol	120	18.45 ± 8.25	5.52e-03 ± 1.75e-03
0.356	14 may 08	786.5590	HARPS-Pol	146	21.14 ± 6.50	1.32e-02 ± 1.43e-03
1.314	14 may 31	809.5840	HARPS-Pol	99	32.36 ± 9.77	7.16e-04 ± 2.20e-03
1.397	14 jun 02	811.5850	HARPS-Pol	120	16.67 ± 7.65	9.20e-04 ± 1.69e-03
1.523	14 jun 05	814.6220	HARPS-Pol	99	−16.66 ± 9.66	−4.61e-03 ± 2.14e-03
1.607	14 jun 07	816.6220	HARPS-Pol	95	−34.92 ± 10.45	−4.82e-03 ± 2.25e-03
1.648	14 jun 08	817.6150	HARPS-Pol	85	−16.75 ± 11.69	−4.24e-03 ± 2.31e-03
1.689	14 jun 09	818.6140	HARPS-Pol	75	−16.33 ± 13.67	−1.93e-03 ± 2.87e-03
1.729	14 jun 10	819.5700	HARPS-Pol	97	−24.67 ± 10.03	−5.63e-03 ± 2.18e-03
1.894	14 jun 14	823.5230	HARPS-Pol	89	1.53 ± 11.60	3.14e-03 ± 2.39e-03
1.935	14 jun 15	824.5230	HARPS-Pol	106	15.89 ± 9.20	5.63e-03 ± 1.96e-03
2.016	14 jun 17	826.4650	HARPS-Pol	113	14.38 ± 8.71	2.82e-03 ± 1.83e-03
2.099	14 jun 19	828.4620	HARPS-Pol	129	22.29 ± 7.44	2.27e-03 ± 1.60e-03
2.144	14 jun 20	829.5330	HARPS-Pol	118	10.17 ± 7.95	6.55e-03 ± 1.76e-03
2.184	14 jun 21	830.5110	HARPS-Pol	114	19.65 ± 8.41	4.76e-03 ± 1.82e-03
2.352	14 jun 25	834.5360	HARPS-Pol	101	40.06 ± 9.60	3.41e-03 ± 2.12e-03
2.643	14 jul 02	841.5440	HARPS-Pol	63	3.14 ± 17.37	2.85e-03 ± 3.50e-03
2.684	14 jul 03	842.5310	HARPS-Pol	101	−18.62 ± 9.72	−5.48e-03 ± 2.08e-03

Table B2. Same as Table B1 for GJ 358.

Cycle	Date	BJD (+2456000)	Instrument	S/N	B (G)	RV (km s^{-1})
0.000	14 jan 17	675.7090	HARPS-Pol	109	−51.09 ± 12.08	−6.39e-03 ± 1.93e-03
0.078	14 jan 19	677.6780	HARPS-Pol	96	−54.90 ± 14.22	−1.23e-03 ± 2.21e-03
0.158	14 jan 21	679.7130	HARPS-Pol	86	−99.91 ± 16.07	−8.14e-04 ± 2.47e-03
0.235	14 jan 23	681.6580	HARPS-Pol	93	−94.82 ± 14.74	−3.57e-03 ± 2.26e-03
0.477	14 jan 29	687.7800	HARPS-Pol	88	−49.06 ± 15.49	−3.10e-03 ± 2.43e-03
0.553	14 jan 31	689.7110	HARPS-Pol	123	−15.37 ± 10.66	5.98e-03 ± 1.68e-03
0.631	14 feb 02	691.6650	HARPS-Pol	121	−1.68 ± 10.99	8.18e-03 ± 1.73e-03
0.789	14 feb 06	695.6510	HARPS-Pol	123	18.37 ± 10.49	4.64e-03 ± 1.71e-03
0.869	14 feb 08	697.6850	HARPS-Pol	113	10.17 ± 11.80	−3.22e-03 ± 1.88e-03
1.468	14 feb 23	712.8430	HARPS-Pol	112	−53.01 ± 11.43	2.75e-03 ± 1.85e-03
1.547	14 feb 25	714.8380	HARPS-Pol	76	−13.01 ± 18.93	9.27e-03 ± 2.86e-03
1.626	14 feb 27	716.8240	HARPS-Pol	107	−8.13 ± 12.01	4.92e-03 ± 1.99e-03
1.704	14 mar 01	718.8090	HARPS-Pol	86	7.23 ± 15.59	−7.48e-04 ± 2.51e-03
1.743	14 mar 02	719.8050	HARPS-Pol	119	12.56 ± 10.58	−2.58e-03 ± 1.78e-03
1.821	14 mar 04	721.7630	HARPS-Pol	124	−9.67 ± 9.97	−1.89e-03 ± 1.70e-03
1.899	14 mar 06	723.7550	HARPS-Pol	109	−29.50 ± 11.70	−4.77e-04 ± 1.96e-03
2.014	14 mar 09	726.6640	HARPS-Pol	106	−49.88 ± 12.37	−5.61e-03 ± 2.02e-03
2.094	14 mar 11	728.6900	HARPS-Pol	133	−81.82 ± 9.12	−9.77e-04 ± 1.56e-03
2.171	14 mar 13	730.6400	HARPS-Pol	86	−83.74 ± 15.55	1.07e-03 ± 2.49e-03
2.645	14 mar 25	742.6240	HARPS-Pol	101	−22.29 ± 12.71	1.19e-02 ± 2.12e-03
2.723	14 mar 27	744.5980	HARPS-Pol	130	12.28 ± 9.45	−1.70e-03 ± 1.60e-03
2.804	14 mar 29	746.6290	HARPS-Pol	107	7.83 ± 11.74	−1.37e-03 ± 1.97e-03
2.880	14 mar 31	748.5630	HARPS-Pol	70	16.42 ± 19.71	−1.72e-03 ± 3.16e-03

Table B3. Same as Table B1 for GJ 205.

Cycle	Date	BJD (+2456000)	Instrument	S/N	B (G)	RV (km s^{-1})
0.000	13 oct 03	569.8850	HARPS-Pol	177	8.29 ± 2.25	−1.05e-05 ± 1.23e-03
0.030	13 oct 04	570.9030	HARPS-Pol	196	11.79 ± 2.00	−4.79e-03 ± 1.12e-03
0.178	13 oct 09	575.8680	HARPS-Pol	228	3.30 ± 1.70	−6.62e-04 ± 8.86e-04
0.208	13 oct 10	576.8910	HARPS-Pol	219	5.16 ± 1.80	9.26e-04 ± 9.94e-04
0.444	13 oct 18	584.8280	HARPS-Pol	188	11.05 ± 2.13	1.51e-03 ± 1.17e-03
0.505	13 oct 20	586.8820	HARPS-Pol	194	4.40 ± 2.04	2.49e-03 ± 1.14e-03
0.682	13 oct 26	592.8720	HARPS-Pol	210	−5.45 ± 1.84	−7.92e-04 ± 1.04e-03
0.741	13 oct 28	594.8510	HARPS-Pol	171	−2.36 ± 2.33	7.87e-04 ± 1.28e-03
0.918	13 nov 03	600.8070	HARPS-Pol	180	6.55 ± 2.20	6.62e-03 ± 1.22e-03
0.977	13 nov 05	602.8160	HARPS-Pol	189	11.98 ± 2.09	1.44e-03 ± 1.07e-03
1.036	13 nov 07	604.7880	HARPS-Pol	197	11.14 ± 2.00	3.71e-03 ± 1.12e-03
1.274	13 nov 15	612.7990	HARPS-Pol	170	2.45 ± 2.36	1.69e-03 ± 1.30e-03
1.332	13 nov 17	614.7790	HARPS-Pol	203	8.53 ± 1.94	−1.66e-03 ± 1.09e-03
1.571	13 nov 25	622.8050	HARPS-Pol	209	2.80 ± 1.88	−4.04e-03 ± 9.73e-04
1.623	13 nov 27	624.5610	NARVAL	313	−1.60 ± 1.31	–
1.630	13 nov 27	624.8090	HARPS-Pol	174	−2.16 ± 2.32	2.68e-03 ± 1.15e-03
1.688	13 nov 29	626.7720	HARPS-Pol	185	−4.40 ± 2.13	−1.92e-03 ± 1.18e-03
1.745	13 dec 01	628.7000	HARPS-Pol	138	−5.52 ± 3.04	2.07e-04 ± 1.57e-03
1.864	13 dec 05	632.6810	HARPS-Pol	171	5.87 ± 2.39	1.84e-03 ± 1.26e-03
2.006	13 dec 10	637.4830	NARVAL	399	8.10 ± 0.97	–
2.065	13 dec 12	639.4620	NARVAL	454	6.75 ± 0.83	–
2.186	13 dec 16	643.5400	NARVAL	308	4.78 ± 1.31	–
3.135	14 jan 17	675.5440	HARPS-Pol	172	4.19 ± 2.42	3.61e-03 ± 1.26e-03
3.197	14 jan 19	677.6080	HARPS-Pol	148	3.78 ± 2.76	7.27e-03 ± 1.59e-03
3.315	14 jan 23	681.5910	HARPS-Pol	133	8.39 ± 3.11	8.42e-03 ± 1.52e-03
3.523	14 jan 30	688.5870	HARPS-Pol	171	5.48 ± 2.37	−4.19e-03 ± 1.27e-03

Table B4. Same as Table B1 for GJ 846.

Cycle	Date	BJD (+2456000)	Instrument	S/N	B (G)	RV (km s^{-1})
0.000	13 sep 10	546.4638	NARVAL	301	2.71 ± 1.43	–
0.637	13 sep 17	553.4688	NARVAL	251	2.14 ± 1.80	–
1.092	13 sep 22	558.4694	NARVAL	282	−1.07 ± 1.57	–
1.269	13 sep 24	560.4200	NARVAL	318	−1.60 ± 1.36	–
2.629	13 oct 09	575.3856	NARVAL	278	3.12 ± 1.57	–
2.821	13 oct 11	577.4947	NARVAL	242	1.67 ± 1.82	–
2.902	13 oct 12	578.3830	NARVAL	297	1.19 ± 1.41	–
2.993	13 oct 13	579.3876	NARVAL	274	−2.93 ± 1.55	–
3.442	13 oct 18	584.3262	NARVAL	209	4.21 ± 2.21	–
4.622	13 oct 31	597.3060	NARVAL	189	2.37 ± 2.44	–
7.075	13 nov 27	624.2851	NARVAL	194	−6.40 ± 2.41	–
8.252	13 dec 10	637.2351	NARVAL	280	1.27 ± 1.57	–
8.434	13 dec 12	639.2356	NARVAL	305	1.98 ± 1.42	–
8.615	13 dec 14	641.2330	NARVAL	234	7.99 ± 1.92	–
8.709	13 dec 15	642.2580	NARVAL	291	4.24 ± 1.52	–
25.764	14 jun 20	829.8720	HARPS-Pol	91	17.14 ± 5.05	8.63e-03 ± 3.26e-03
25.950	14 jun 22	831.9170	HARPS-Pol	158	7.85 ± 2.62	1.08e-03 ± 1.78e-03
26.132	14 jun 24	833.9110	HARPS-Pol	140	8.96 ± 3.02	−9.73e-05 ± 2.15e-03
26.314	14 jun 26	835.9120	HARPS-Pol	100	2.19 ± 4.55	2.84e-03 ± 3.03e-03
28.311	14 jul 18	857.8880	HARPS-Pol	111	6.47 ± 4.01	1.08e-02 ± 2.93e-03
28.398	14 jul 19	858.8430	HARPS-Pol	141	−0.08 ± 2.96	8.27e-03 ± 2.00e-03
28.493	14 jul 20	859.8910	HARPS-Pol	129	2.69 ± 3.34	5.13e-03 ± 2.15e-03
28.761	14 jul 23	862.8310	HARPS-Pol	107	6.86 ± 7.38	8.41e-03 ± 2.78e-03
28.850	14 jul 24	863.8130	HARPS-Pol	119	10.93 ± 3.61	1.04e-02 ± 2.31e-03
28.940	14 jul 25	864.8020	HARPS-Pol	131	4.41 ± 3.28	9.71e-03 ± 1.98e-03
31.849	14 aug 27	896.8010	HARPS-Pol	102	−0.01 ± 4.45	5.91e-03 ± 2.70e-03

Table B5. Same as Table B1 for GJ 410.

Cycle	Date	BJD (+2456000)	Instrument	S/N	B (G)	RV (km s^{-1})
0.558	14 jan 09	667.6948	NARVAL	282	−8.94 ± 1.50	–
0.696	14 jan 11	669.6198	NARVAL	255	5.28 ± 1.69	–
1.000	14 jan 15	673.8840	HARPS-Pol	90	16.52 ± 5.62	−1.97e-02 ± 3.85e-03
1.928	14 jan 28	686.8660	HARPS-Pol	84	27.53 ± 6.11	−2.79e-03 ± 4.41e-03
1.996	14 jan 29	687.8170	HARPS-Pol	79	8.28 ± 6.59	4.17e-03 ± 4.34e-03
2.067	14 jan 30	688.8200	HARPS-Pol	108	4.11 ± 4.55	−5.30e-04 ± 2.90e-03
2.209	14 feb 01	690.8100	HARPS-Pol	112	3.32 ± 4.35	1.31e-02 ± 3.06e-03
2.281	14 feb 02	691.8190	HARPS-Pol	103	−1.09 ± 4.75	9.54e-04 ± 3.32e-03
2.423	14 feb 04	693.7960	HARPS-Pol	110	−15.13 ± 4.41	2.79e-03 ± 3.08e-03
2.493	14 feb 05	694.7790	HARPS-Pol	106	−13.66 ± 4.66	3.50e-03 ± 3.23e-03
2.565	14 feb 06	695.7870	HARPS-Pol	109	−8.80 ± 4.45	6.28e-03 ± 3.13e-03
2.707	14 feb 08	697.7710	HARPS-Pol	100	10.94 ± 4.92	−2.21e-02 ± 3.40e-03
3.777	14 feb 23	712.7580	HARPS-Pol	123	34.21 ± 3.85	−2.86e-03 ± 2.59e-03
3.849	14 feb 24	713.7600	HARPS-Pol	107	30.37 ± 4.53	2.02e-03 ± 2.94e-03
3.992	14 feb 26	715.7630	HARPS-Pol	122	19.46 ± 3.86	−3.82e-03 ± 2.82e-03
4.133	14 feb 28	717.7440	HARPS-Pol	101	3.45 ± 4.82	4.44e-03 ± 3.37e-03
4.278	14 mar 02	719.7690	HARPS-Pol	125	−2.65 ± 3.82	2.06e-02 ± 2.52e-03
4.347	14 mar 03	720.7430	HARPS-Pol	118	−7.61 ± 4.02	8.56e-03 ± 2.69e-03
4.418	14 mar 04	721.7260	HARPS-Pol	103	−1.61 ± 4.73	8.66e-03 ± 3.61e-03
4.630	14 mar 07	724.7060	HARPS-Pol	98	9.48 ± 5.00	1.01e-03 ± 3.52e-03
4.703	14 mar 08	725.7160	HARPS-Pol	94	24.12 ± 5.32	2.93e-03 ± 3.62e-03
4.776	14 mar 09	726.7450	HARPS-Pol	108	16.25 ± 4.47	2.14e-03 ± 3.17e-03
4.845	14 mar 10	727.7130	HARPS-Pol	113	22.17 ± 4.30	−2.84e-03 ± 3.05e-03
4.988	14 mar 12	729.7070	HARPS-Pol	112	9.37 ± 4.23	−1.80e-04 ± 2.84e-03
5.058	14 mar 13	730.6860	HARPS-Pol	89	6.96 ± 5.69	−6.63e-03 ± 3.84e-03
5.130	14 mar 14	731.6960	HARPS-Pol	83	7.69 ± 6.25	−5.06e-03 ± 4.48e-03
5.769	14 mar 23	740.6520	HARPS-Pol	103	16.34 ± 4.84	−5.91e-03 ± 3.06e-03
5.913	14 mar 25	742.6630	HARPS-Pol	113	11.95 ± 4.27	2.96e-03 ± 2.85e-03
6.036	14 mar 27	744.3780	NARVAL	169	11.67 ± 2.85	–
6.055	14 mar 27	744.6480	HARPS-Pol	97	5.46 ± 5.06	−8.96e-03 ± 3.52e-03
6.127	14 mar 28	745.6580	HARPS-Pol	110	6.51 ± 4.45	−1.39e-02 ± 3.09e-03
6.199	14 mar 29	746.6660	HARPS-Pol	124	−3.10 ± 3.82	1.81e-03 ± 2.76e-03
6.753	14 apr 06	754.4280	NARVAL	221	11.83 ± 2.09	–
6.899	14 apr 08	756.4720	NARVAL	298	11.17 ± 1.43	–
6.969	14 apr 09	757.4440	NARVAL	303	7.82 ± 1.42	–
7.119	14 apr 11	759.5440	NARVAL	262	4.32 ± 1.73	–
7.184	14 apr 12	760.4620	NARVAL	281	1.66 ± 1.53	–
7.255	14 apr 13	761.4560	NARVAL	296	−0.22 ± 1.47	–
7.323	14 apr 14	762.4040	NARVAL	229	−2.88 ± 1.91	–
7.399	14 apr 15	763.4680	NARVAL	294	−6.74 ± 1.47	–
7.468	14 apr 16	764.4370	NARVAL	300	−7.45 ± 1.45	–
7.542	14 apr 17	765.4620	NARVAL	253	−4.75 ± 1.76	–

APPENDIX C: SUPPLEMENTARY B_l DATA

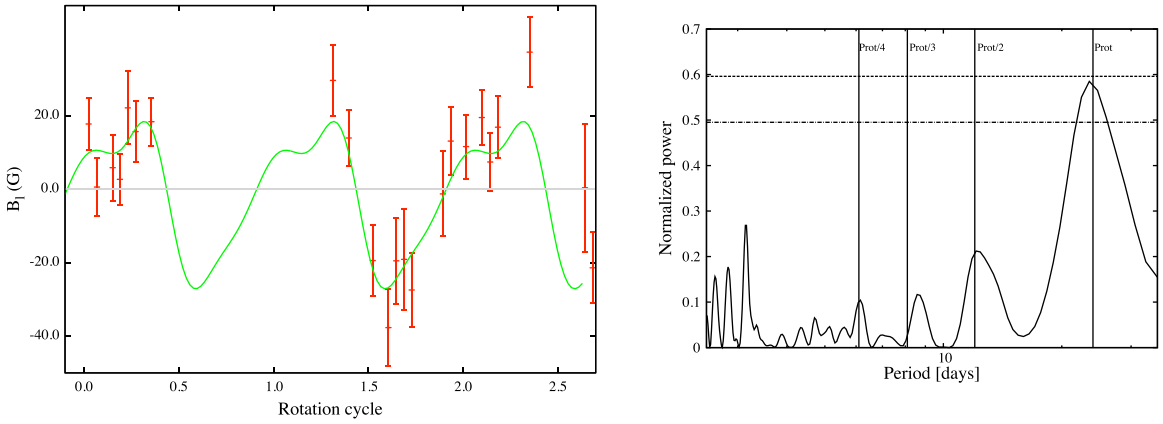

Figure C1. Same as Fig. 1 for GJ 479.

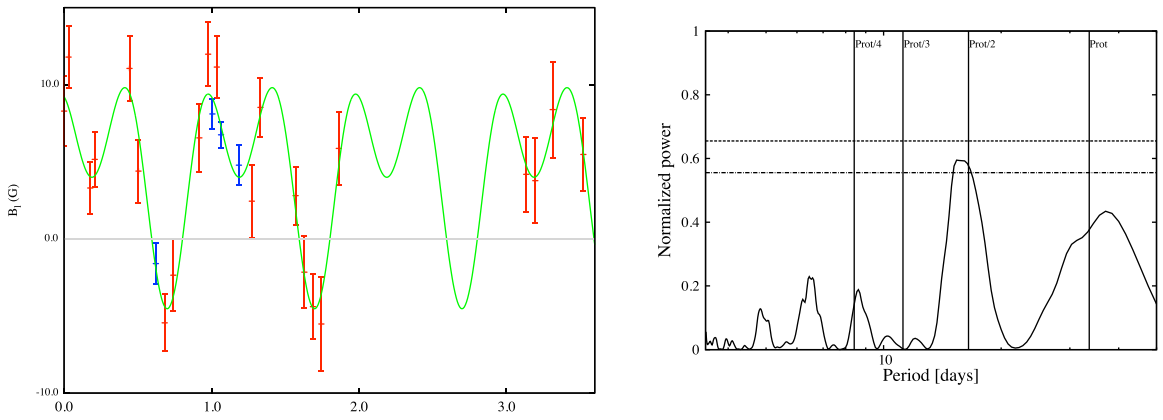

Figure C2. Same as Fig. 1 for GJ 205. HARPS-Pol data are in red, NARVAL data are in blue.

APPENDIX D: SUPPLEMENTARY STOKES *V* LSD PROFILES AND PARENT LARGE-SCALE MAGNETIC FIELD MAPS

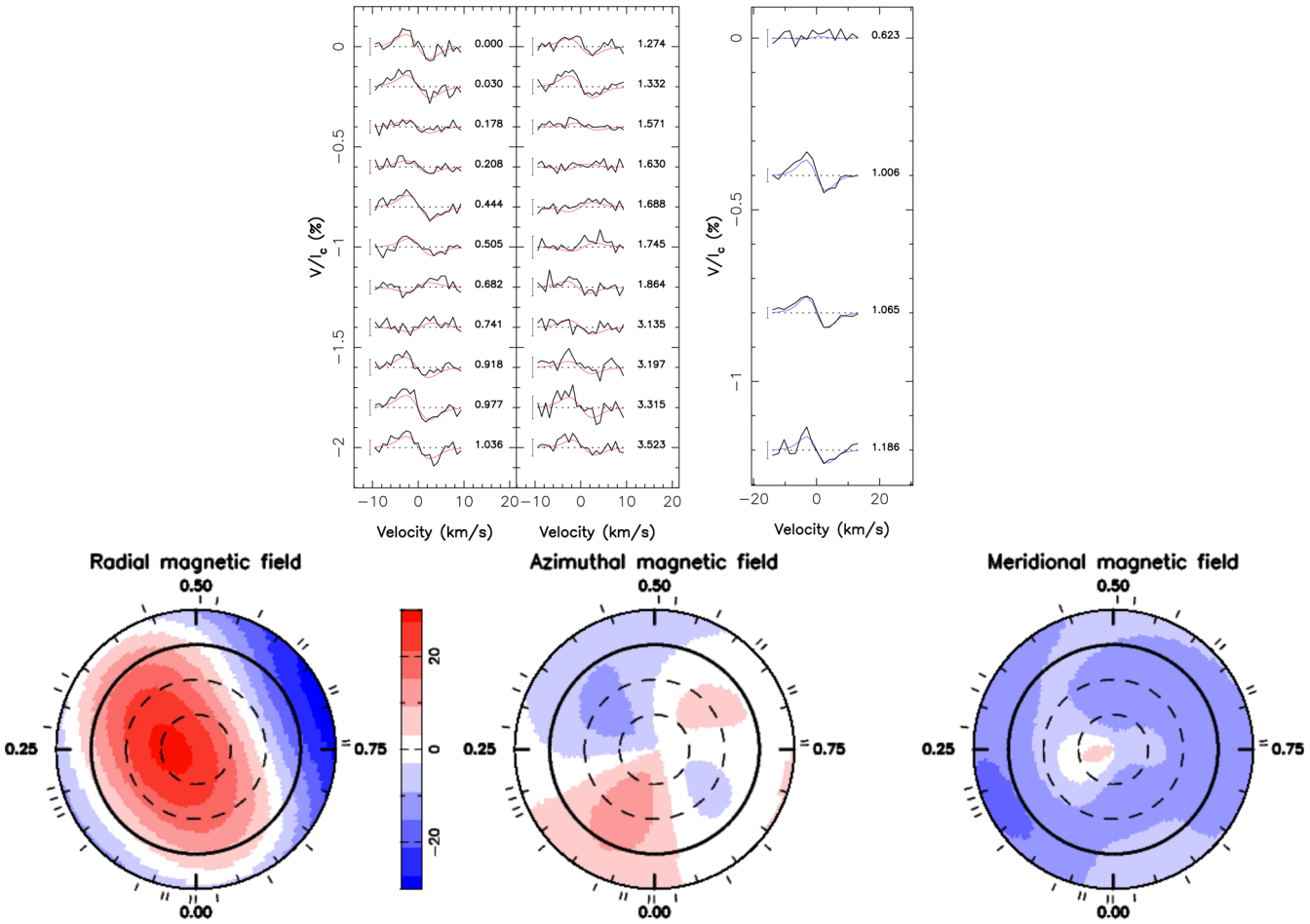

Figure D1. Same as Fig. 3 for GJ 205. LSD Stokes *V* profiles in the top-left and top-right panels correspond to HARPS-Pol and NARVAL observations, respectively.

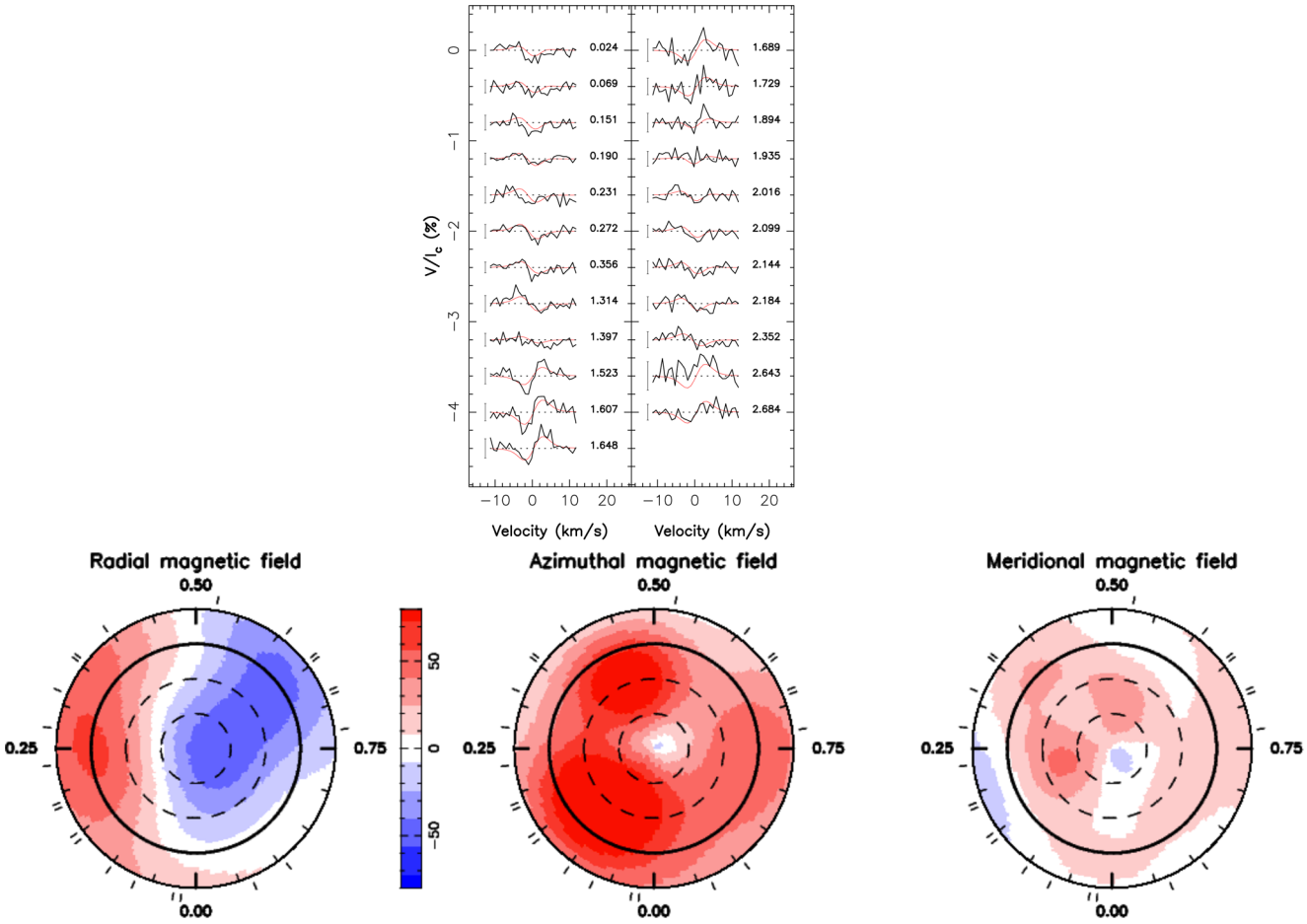

Figure D2. Same as Fig. 3 for GJ 479.

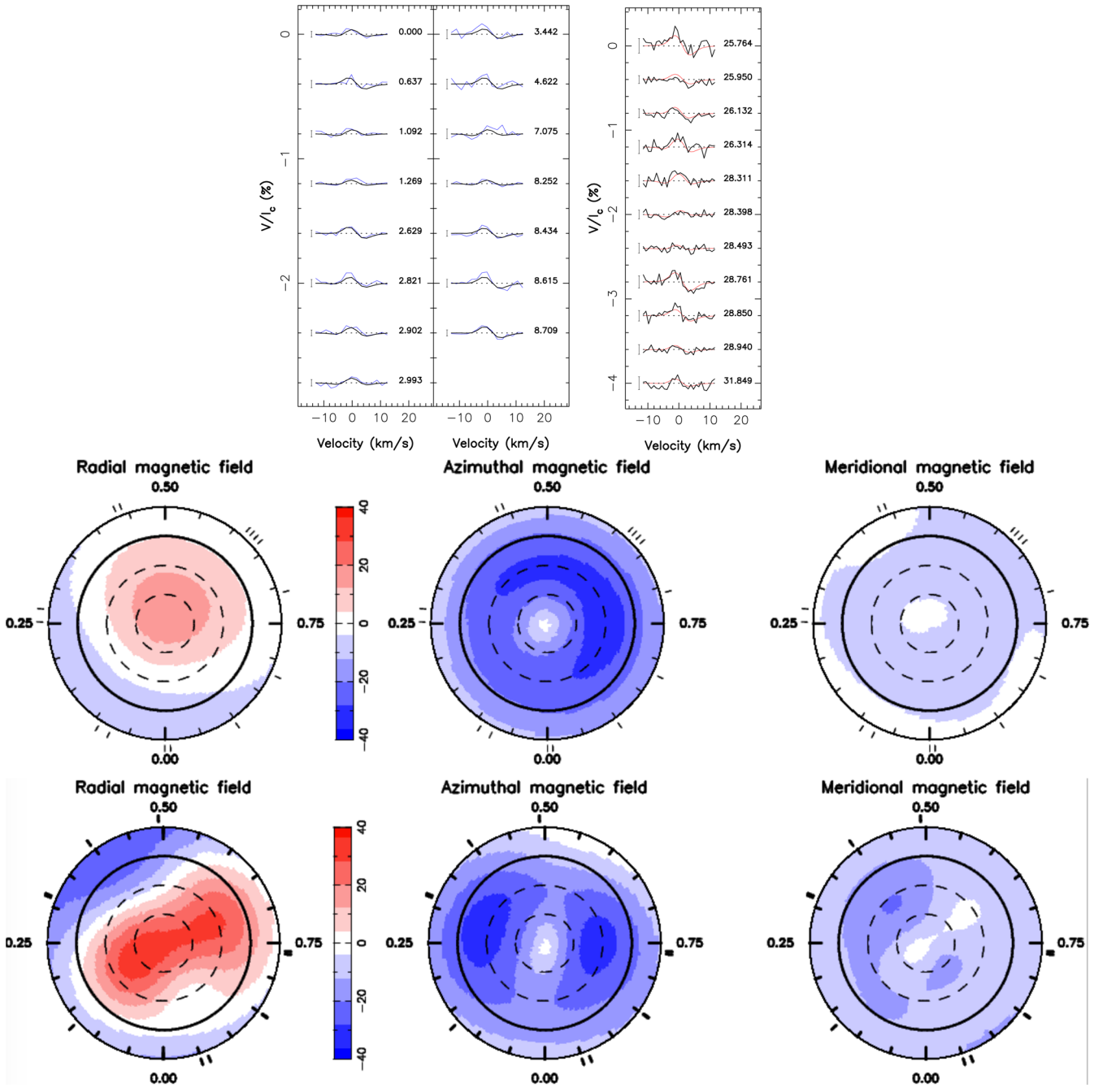

Figure D3. Same as Fig. 3 for GJ 846. LSD Stokes *V* profiles in the top-left and top-right panels correspond toNARVAL and HARPS-Pol observations, respectively.

APPENDIX E: SUPPLEMENTARY B_l, v_r, FWHM, Hα AND v_s DATA

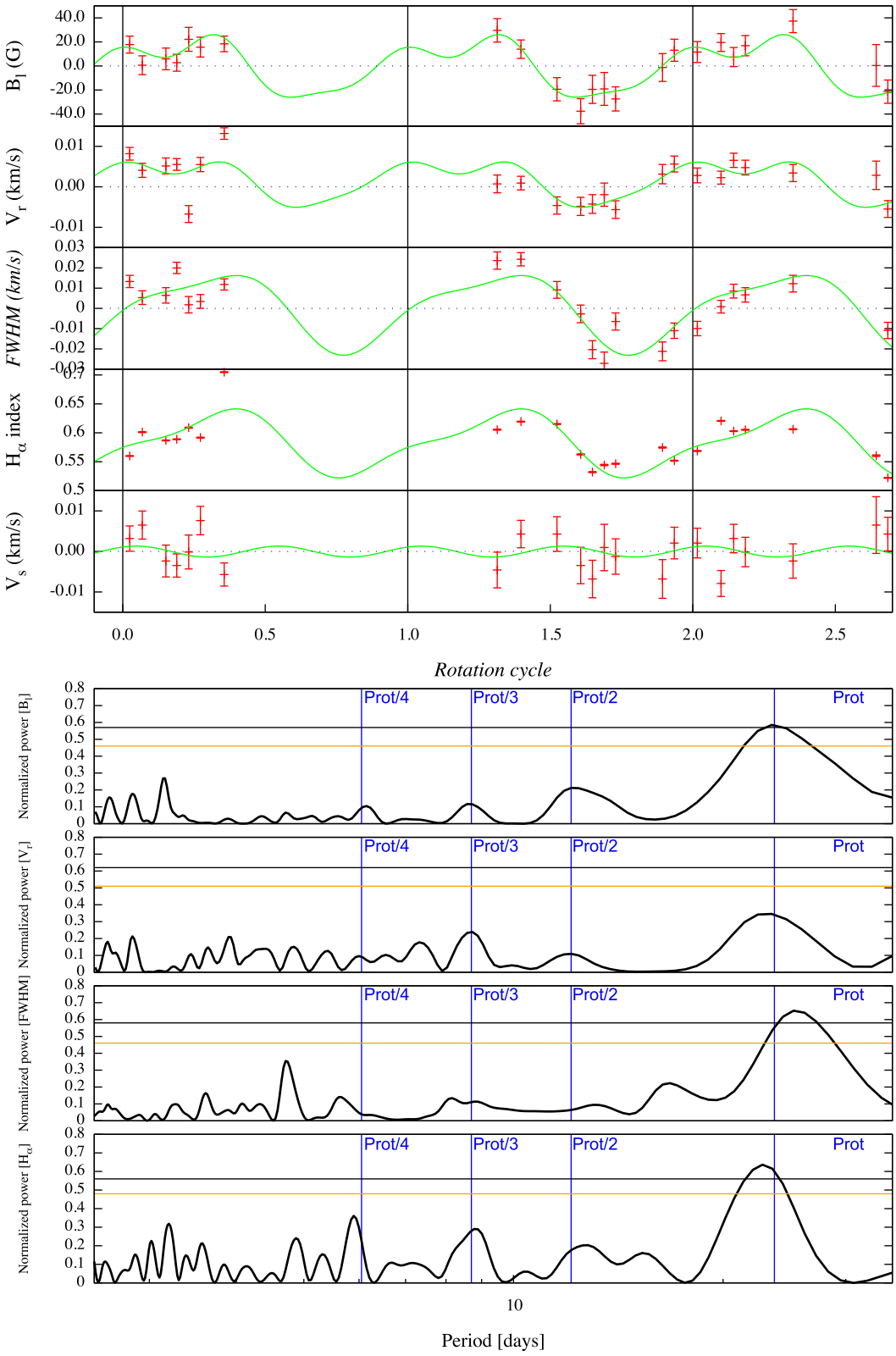

Figure E1. As Fig. 6 for GJ 479.

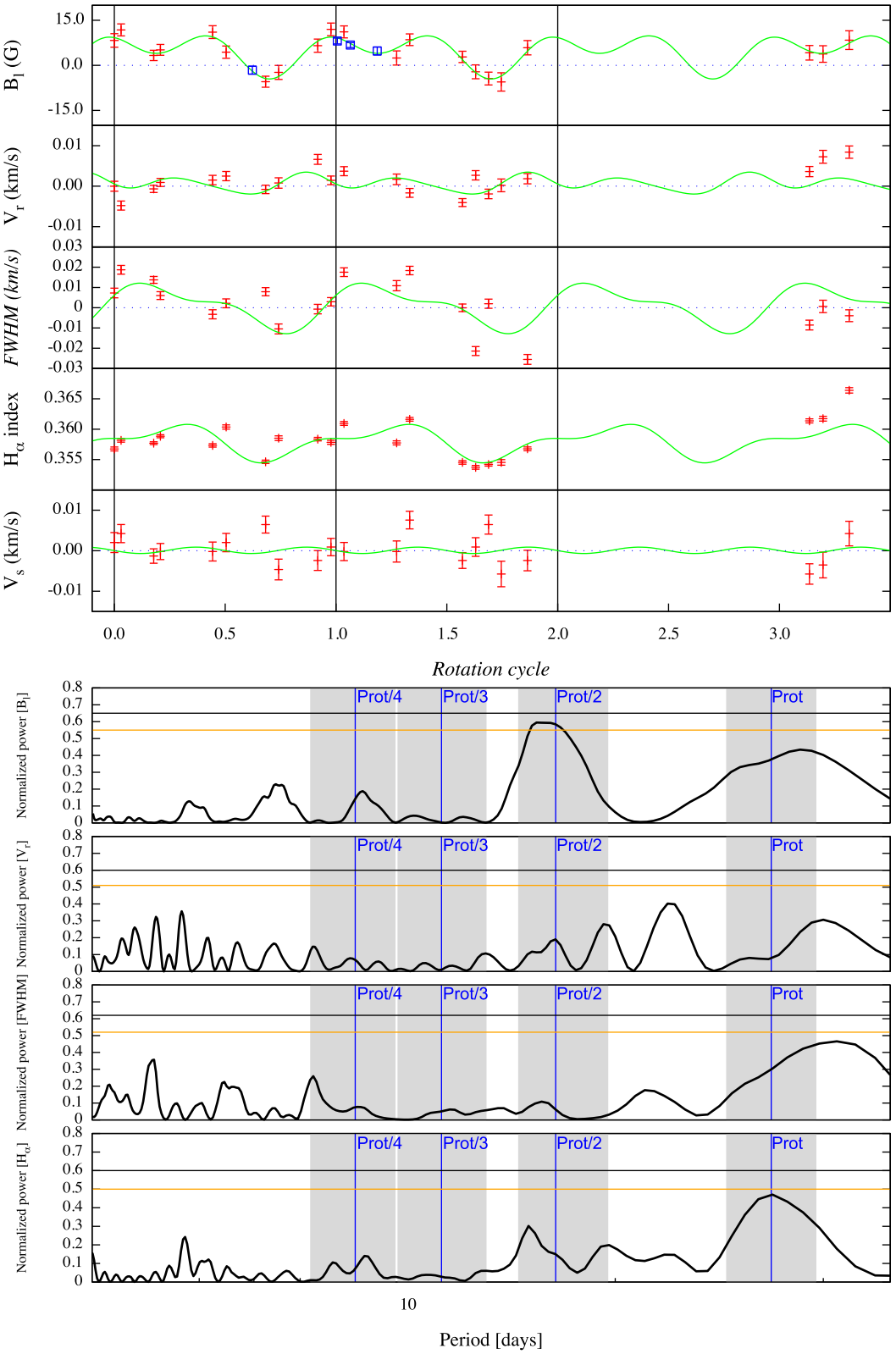

Figure E2. As Fig. 7 for GJ 205. Note that for this star, the DR is supposed only, and not measured from the data set.

APPENDIX F: COMPLEMENTARY RESULTS OF THE SIMULATIONS PRESENTED IN SECTION 5.2

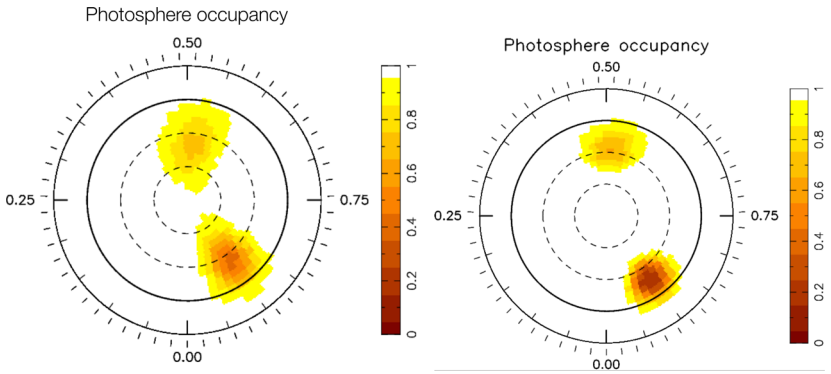

Figure F1. Reconstructed map obtained for a star with $v \sin i = 1$ km s^{-1} and $i = 60°$ with two spots covering 1.5 per cent of the stellar surface. Left: reconstructed map from *I* with the sampling A, Right: reconstructed map from *RI* with the sampling A, The colour scale depicts the photosphere filling factor of each cell (white corresponding to a unspotted cell).

APPENDIX G: SUPPLEMENTARY *RI* SPECTRA

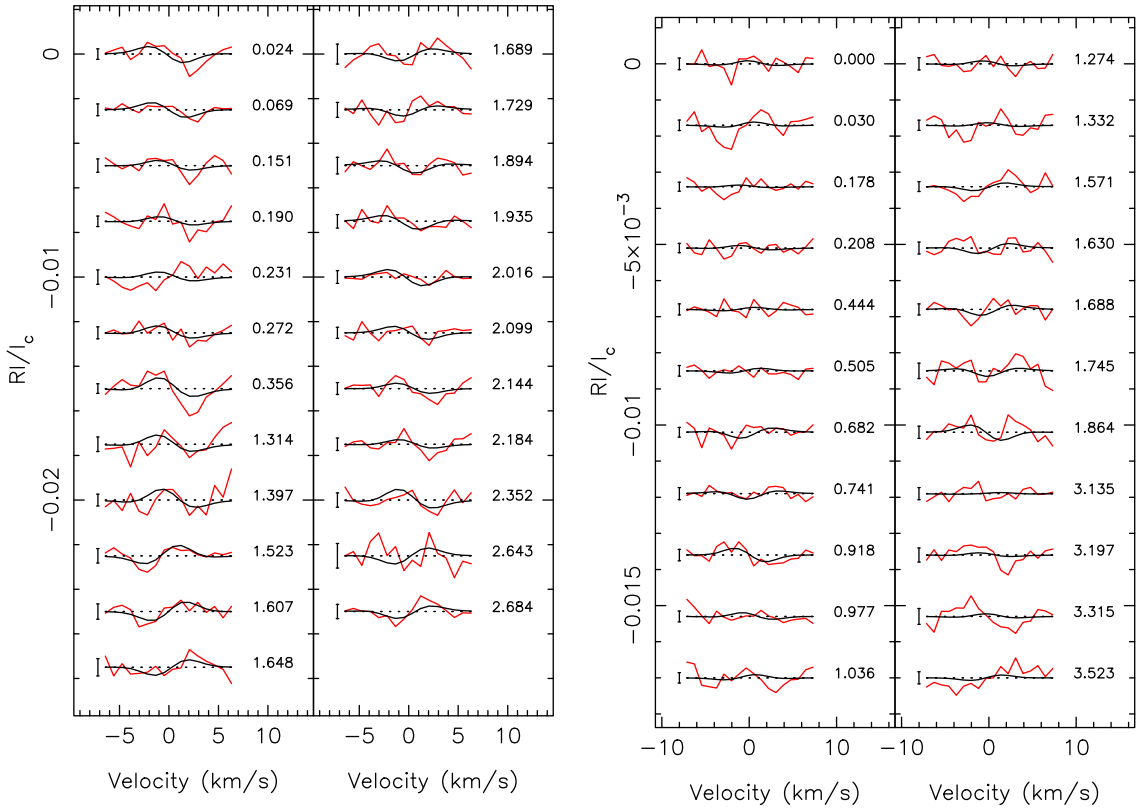

Figure G1. Same as Fig. 9 for GJ 479 (left) and GJ 205 (right).

APPENDIX H: SUPPLEMENTARY B_l, v_r AND FWHM RECONSTRUCTION, AND RELATIVE BRIGHTNESS MAPS

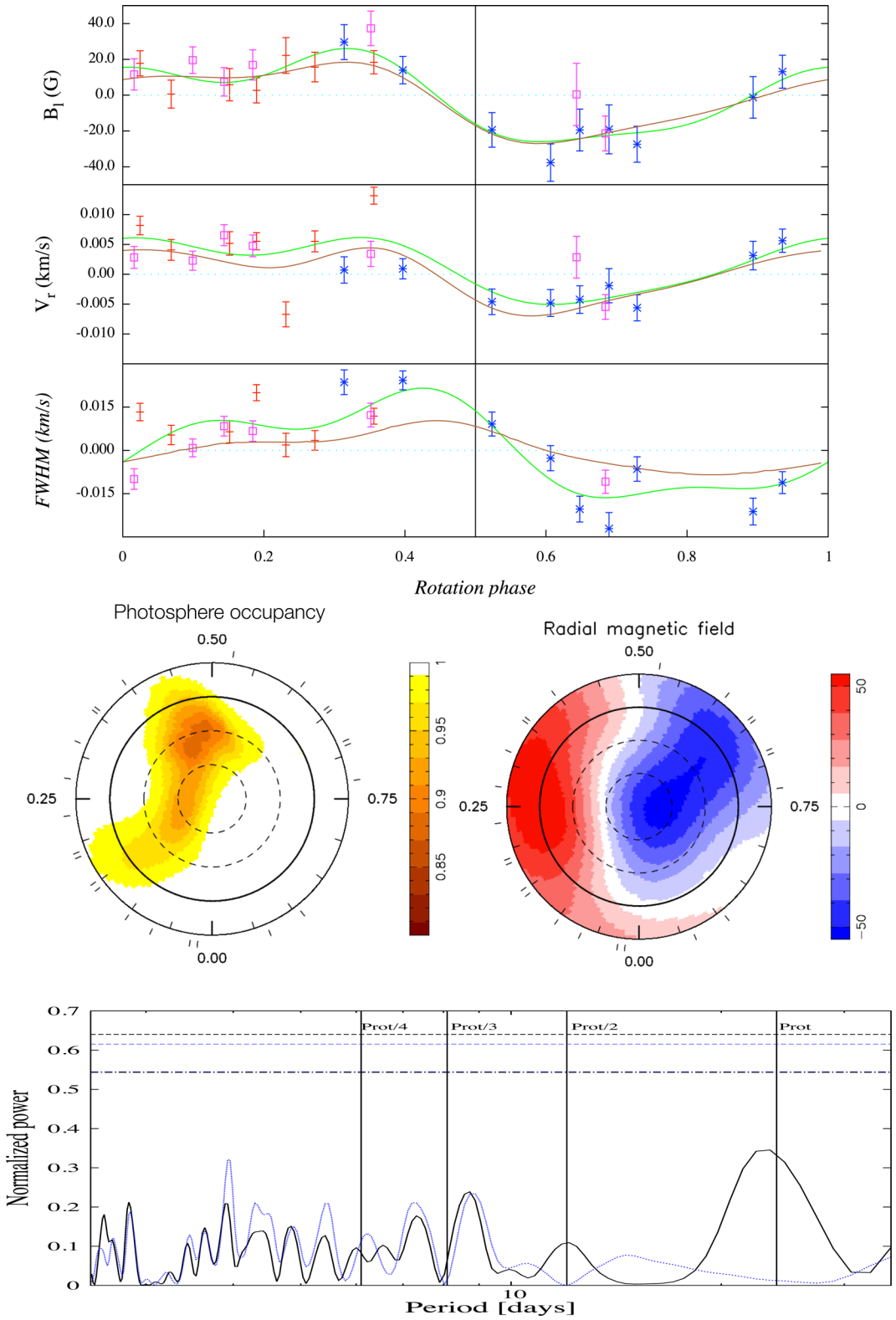

Figure H1. Same as Fig. 10 for GJ 479.

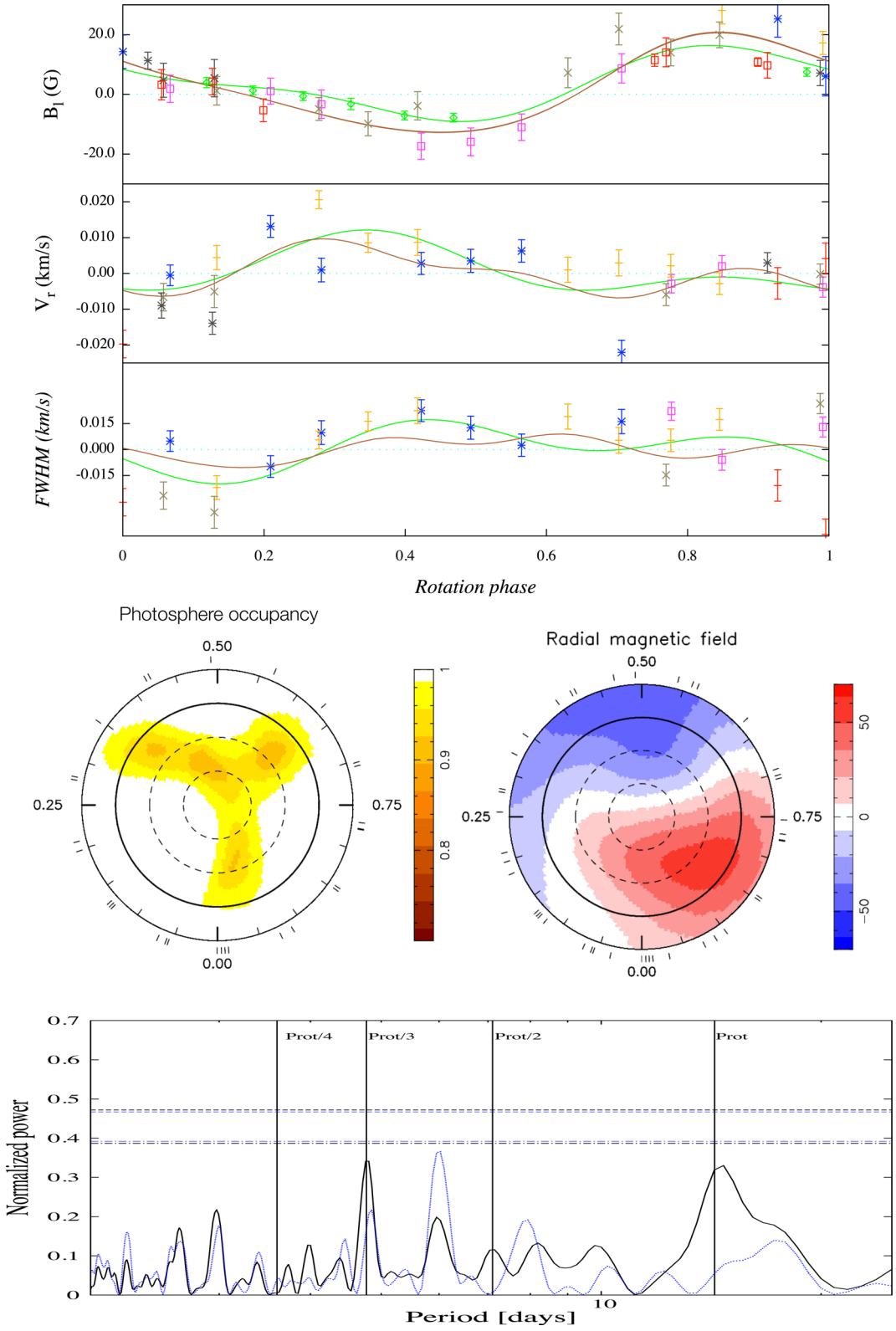

Figure H2. Same as Fig. 10 for GJ 410, from the whole data set.

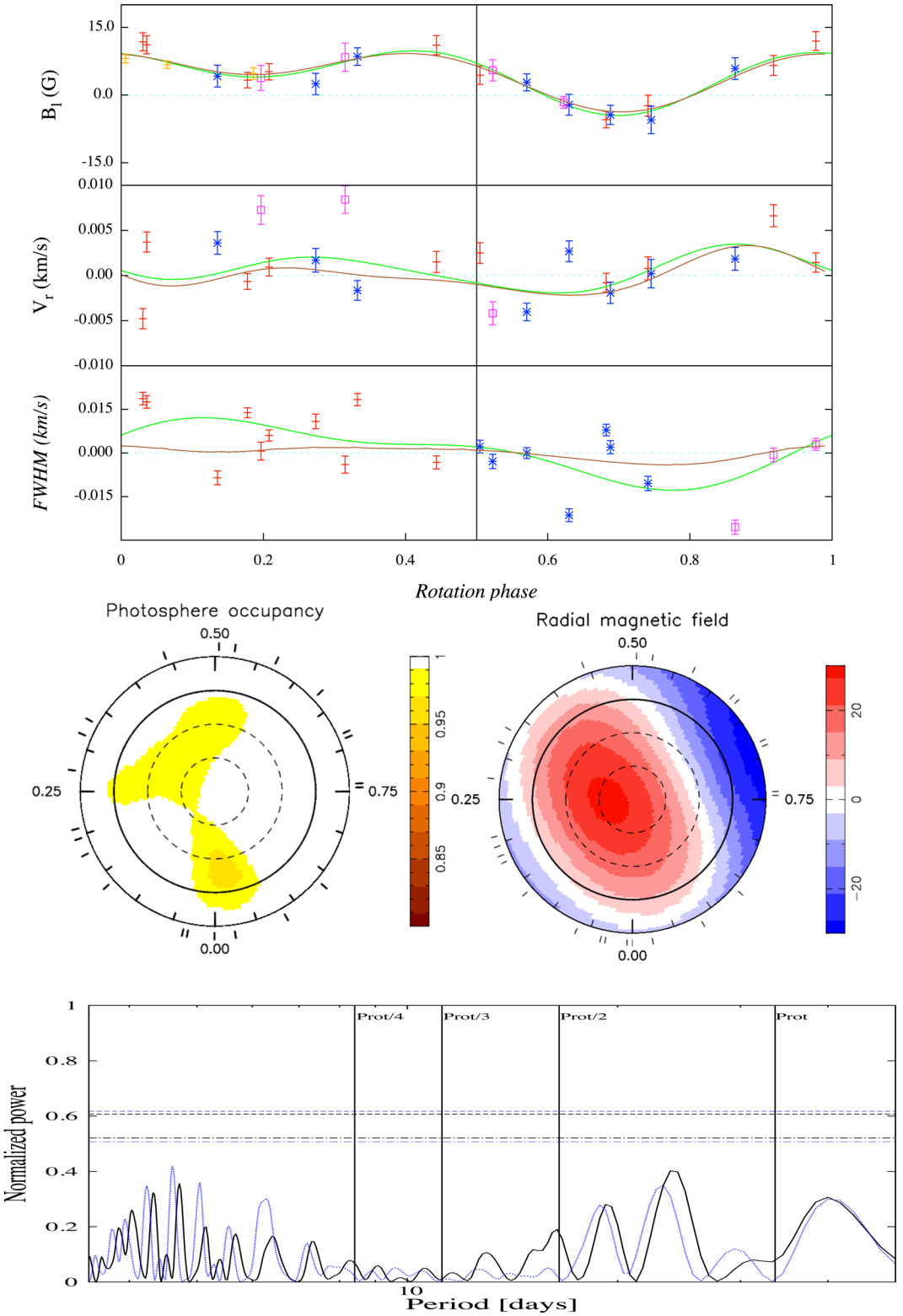

Figure H3. Same as Fig. 10 for GJ 205.

This paper has been typeset from a TEX/LATEX file prepared by the author.